Molecular Dynamics Simulation of Nano-indentation Studies on Zr-based Metallic Glass Matrix Composites

A thesis submitted in partial fulfilment of the
requirements for the degree of

Master of Technology (Research)

in

Metallurgical and Materials Engineering

by

ASHWANI KUMAR

(Roll No-612MM1009)

Department of Metallurgical and Materials Engineering
National Institute Of Technology, Rourkela
October, 2015

Molecular Dynamics Simulation of Nano-indentation Studies on Zr-based Metallic Glass Matrix Composites

A thesis submitted in partial fulfilment of the requirements for the degree of

Master of Technology (Research)

in

Metallurgical and Materials Engineering

by

ASHWANI KUMAR

(Roll No-612MM1009)

Under the supervision of

Dr. Natraj Yedla
Assistant Professor
and
Dr. Syed Nasimul Alam
Assistant Professor

Department of Metallurgical and Materials Engineering
National Institute Of Technology, Rourkela
October, 2015

Dedicated

To

My Parents

&

Lord Shiva

APPROVAL OF THE VIVA-VOCE BOARD

DD/MM/YR

Certified that the thesis entitled "**Molecular Dynamics Simulation of Nano-Indentation studies on Zr-based Metallic Glass Matrix Composites",** submitted by **ASHWANI KUMAR** to National Institute of Technology, Rourkela, for the award of the degree of Master of Technology (Research) has been accepted by the external examiners and that the student has successfully defended the thesis in the viva-voce examination held today.

Prof. A. K. Mondal
(Member of the MSC)

Prof. T. Roy
(Member of the MSC)

Prof. S. K. Panda
(Member of the MSC)

Prof. Natraj Yedla
(Supervisor)

Prof. S. N. Alam
(Co-Supervisor)

Name:
(External Examiner)

Prof. S.C. Mishra
(Chairman)

Department of Metallurgical and Materials Engineering
National Institute Of Technology, Rourkela
Rourkela-769008, Odisha, India

CERTIFICATE

This is to certify that the thesis entitled, "**Molecular Dynamics Simulation of Nano-Indentation studies on Zr-based Metallic Glass Matrix Composites"** submitted by **Ashwani Kumar (612MM1009)** in partial fulfilment of the requirement for the award of Master of Technology (Research) in **Metallurgical and Materials Engineering Department** at the National Institute of Technology, Rourkela is a bonafide record of research work carried out by him under our supervision and guidance. To the best of my knowledge, the matter embodied in the thesis is based on candidate's own work, has not been submitted to any other university / institute for the award of any degree or diploma.

Date:
Place:

Dr. Natraj Yedla
Assistant professor
Dept. of Metallurgical and Materials Engg.
National Institute of Technology
Rourkela – 769008
Odisha, India

Dr. Syed Nasimul Alam
Assistant professor
Dept. of Metallurgical and Materials Engg.
National Institute of Technology
Rourkela – 769008
Odisha, India

ACKNOWLEDGEMENT

This work would not have been possible without the support from **NIT, ROURKELA**. I want to express my utmost gratitude to my supervisor, **Dr. NATRAJ YEDLA and Dr. SYED NASIMUL ALAM** for their support, both intellectual and emotional, throughout the years of my M.Tech (Research) studies. They took me from my infantile knowledge of Material Science and introduced me to a whole new world. Performing simulation work with them left me in both joy and awe and I hope to retain this excitement in any future research endeavour. It was through their encouragement and understanding that I am standing here today, about to embark on a career in academia. I want to thank them for all the time they spent with me explaining the most obscure concepts, for helping me to view results with a whole new light and for teaching me how to think by myself. I hope that one day I may be able to repay them for all the good they have done for me.

I would also like to express my utmost gratitude to **Prof. S.C. Mishra, HOD, Metallurgical & Materials Engineering Department** for allowing me to use the departmental facilities and for his valuable suggestions and encouragement at various stages of the work. I also want to thank my friends Pradeep and Trinath who had always encouraged and supported in doing my work. I would like to thank all the staff members of Department of Metallurgical & Materials Engineering who had been very cooperative with me at all times. Finally, I would like to express my deepest gratitude to my parents for their unconditional love and encouragement. I would not be where I am today without the support of them.

Metallurgical & Materials Engineering Deptt. (**Ashwani Kumar)**
NIT, Rourkela, Odisha, India
Date:

DECLARATION

I certify that

a. The work contained in this thesis is original and has been done by me under the guidance of my supervisor.
b. The work has not been submitted to any other Institute for any degree or diploma.
c. I have followed the guidelines provided by the Institute in preparing the thesis.
d. I have conformed to the norms and guidelines given in the Ethical Code of Conduct of the Institute.
e. Whenever I have used materials (data, theoretical analysis, and text) from other sources, I have given due credit to them by citing them in the text of the thesis and giving their details in the references.
f. Whenever I have quoted written materials from other sources, I have put them under quotation marks and given due credit to the sources by citing them and giving required details in the references.

Signature of the Student

LIST OF FIGURES

LIST OF TABLES

Abstract

In the present investigation molecular dynamics (MD) simulations of nano-indentation on $Zr_{50}Cu_{50}$, $Zr_{50}Cu_{30}Al_{20}$ metallic glasses (MGs) and $Zr_{50}Cu_{50}$, $Zr_{50}Cu_{30}Al_{20}$ glass matrix composites (GMCs) with 14%, 30% and 50% crystalline volume fraction have been studied. Nano-indentation tests are conducted at varying strain rates (2.5×10^{9} s^{-1}, 2.5×10^{10} s^{-1}, 1.25×10^{11} s^{-1} and 2.5×10^{11} s^{-1}) and temperatures (100K, 300K and 500K) to investigate the deformation behaviour and response on the mechanical properties such as yield point, maximum load, and hardness through load-displacement plots. Also, the effect of crystallite distribution (single-spherical and multi-spherical) and shape (spherical and cylindrical) on the load-displacement response have been studied. Structural analysis during deformation has been done by centro-symmetry parameter (CSP) studies. It is found that all curves have linear elastic behaviour and non-linear plastic behaviour with load varying linearly with displacement of the indenter following Hertz's contact theory in the elastic region. After the first "pop in" or initiation of plastic deformation, serrations are observed to be irregularly spaced in amorphous alloys because of their short range order arrangement of atoms. With increase of strain rate, yield point and maximum load occur at higher loads in GMCs as compared to that of MGs. This may be due to delay in load transfer from amorphous phase to crystallites which can be observed in the atomic position snapshots of CSP studies. The increase of temperature leads to the decrease in the yield point and maximum loads in MG and GMCs. This may be due to the fact that atoms are displaced far away and so the inter-atomic interaction force decreases causing softening of the alloy. Studies on the effect of crystallite distribution show that single-crystallite (14%) reinforced composite exhibits higher strength as compared to multi-spherical crystallite composite (14%). Also, studies on the shape of the crystallite reveal that composite reinforced with cylindrical shaped crystallites (14%) offer better strength than that of the composite with spherical crystallites (14%). From this study, it can be concluded that GMCs have better strength compared to MGs. $Zr_{50}Cu_{50}$ with 30 % crystalline volume fraction has better strength and in case of $Zr_{50}Cu_{30}Al_{20}$ GMC with 50% crystalline volume fraction exhibits superior properties.

Key words: Molecular Dynamics simulation, nano-indentation, Load-displacement plots, CSP analysis, strain rate, temperature, yield point

CONTENTS

CHAPTER 1

INTRODUCTION

1.1. Background

A metallic glass (amorphous metal) is an alloy of metals having a disordered atomic structure [1]. Duwez and co-workers at Caltech laboratory were first to prepare the metallic glass ($Au_{75}Si_{25}$) by rapid quenching technique in 1960 [2]. Structural application of metallic glass (MG) was not feasible until the development of bulk metallic glass in 1990's pioneered by research groups of Inoue at Tohoku University in Japan and Johnson at California Institute of Technology in the U.S [3, 4]. BMGs have been used for many structural applications because of their typical mechanical properties as compared to the crystalline materials like large elastic strain limit (~2 %), good corrosion resistance, higher strength(2GPa), and higher hardness [5–7]. But they exhibit limited plasticity in compression (0-2 %) and negligible in tension (<0.5 %) leading to catastrophic failure and thus restricted area of use [5, 8, 9]. There are several types of BMGs such as Cu-based, Zr-based, Ti based, Fe-based [10]. The most widely studied are Cu-based metallic glass as they have good glass forming ability, high thermal stability, high corrosion resistance and high strength [10]. BMGs have a distinct deformation mechanism as compared to the crystalline materials due to the absence of defects such as dislocations. The deformation studies revealed that at low strain rate, BMGs fail in discrete manner by shear banding which results in brittle failure while this deformation becomes continuous at high strain rates and not in discrete manner. This is due to the formation of a single shear band at low strain rate which is not able to bear sudden high strain values so multiple shear bands are formed at higher strain rates [11]. To improve the ductility, BMG composites were synthesized. It was found that there was significant increase in the plastic strain due to the obstruction of the rapid propagation of shear bands in the presence of crystallites [8, 9]. Several deformation studies were done on BMG reinforced with crystalline particulates [6, 12]. It was found that addition of reinforcement changed their mechanical properties such as fracture toughness, and ductility by formation of multiple shear bands. Addition of Nb to $Zr_{57}Nb_5Al_{10}Cu_{15.4}Ni_{12.6}$ BMG to form composite increased its toughness [6]. Wang et al. [13] did experiments to show that the addition of Nb resulted in increase of ductility of the Zr-Ti-Cu-Ni-Be metallic glass system due to formation of crystalline phases. As stated earlier the deformation mechanism in glasses is different to that of crystalline materials because of their disordered atomic structure. There are several proposed deformation mechanism theories, such as STZ (shear transformation zone), shear band theory and free volume theory. As proposed by Argon [14] STZ is the fundamental unit of plastic deformation of metallic glasses similar to dislocation in crystalline materials. Further, STZ are local cluster of atoms which of few nanometres that reorganise by the application of shear stress. This involves s dislocation of atoms, their inelastic rearrangement and redistribution of shear transformation around free volume regions. A distinct theory for deformation mechanism of metallic glasses was anticipated by Spaepen [15]. Metallic glasses comprise of free volume and plastic deformation occurs by creation of free volume and its destruction by diffusion.

1.2. Motivation for the present study

Extensive studies using classical molecular dynamics (MD) have been carried out to understand the stress-strain characteristics and atomistic mechanism of plastic deformation in Cu-Zr based metallic glasses [16–19]. However, there are seldom simulation studies reported on the deformation behaviour of Zr-based MGs and GMCs. Also, the structural transformation during deformation, influence of crystallite shape, volume fraction and distribution in GMCs is not reported. MD simulation is generally believed to be an effective way in modelling various indentation processes [16], providing an in situ observation on atomic motions.

1.3. Organization of thesis

This chapter (Chapter 1) provides a brief introduction of the present work along with its primary objectives and a brief look at the gaps in the experimental and MD simulation studies on deformation of Zr-Cu based metallic glass and Zr-Cu based glassy alloys containing crystallites. Chapter 2 presents a literature review on the subject matter of glass forming ability, processing routes of metallic glasses, types of metallic glasses, deformation mechanisms in metallic glasses, effect of Al addition on the deformation behaviour of Zr-Cu metallic glasses and its composites, effect of strain rate and MD simulations on the deformation behaviour of Zr-Cu glass and glass composites. Comparison of mechanical properties of Zr-Cu based metallic glass and composites under experimental and simulation studies. These are followed by gaps in the literature and finally the brief aims and objectives of the present study. In Chapter 3, a brief description of classical molecular dynamics simulation procedure, modelling using LAMMPS software and plan showing the details of simulation studies is given. Chapter 4 is about (a) results of molecular dynamics simulation studies and (b) discussions based on the observed results. Chapter 5 presents the conclusions of this study and scope for future work.

CHAPTER 2

LITERATURE REVIEW

2.1. Introduction to metallic glasses

Glass may have typically any available type of bonding i.e., metallic, covalent, ionic, hydrated ionic and molecular [20]. Amorphous metals or metallic glass do not contain long range periodicity as found in crystals (Figs. 2.1a and 2.1b). Unlike common glasses like window glass, which are normally insulators, metallic glasses have good electrical conductivity. Metallic glasses are opaque while common glasses (silicon glasses) are transparent [21]. When the metallic glasses have a critical casting thickness of 1 cm or more and have three or more alloys mixed together, are termed as bulk metallic glass [22]. Amorphous metals have good electrical conductivity, good forming and shaping ability, large elastic strain limit, high yield strength, high hardness, good corrosion resistance, resistance to wear (due to absence of grain boundary), glass transition (it gradually softens, changing from solid to liquid over a range of temperature, very useful for processing glass into complex shapes), resistance to plastic deformation (due to higher viscosity than metals and alloys, which prevents atoms moving enough to form ordered lattice) [5–7, 23], but lower ductility and fatigue strength than polycrystalline metal alloys [5, 8, 9]. The presence of crystalline phase in BMG as reinforcement or precipitate leads to formation of glass matrix composites (GMC). According to some researchers the presence of crystalline phase leads to enhancement of ductility of BMGs by restraining the shear band propagation [24, 25].

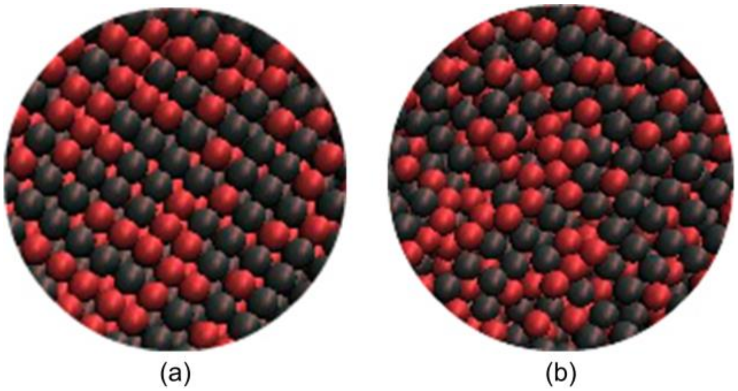

Fig. 2.1. Atomic snapshots: (a) crystalline structure (b) amorphous structure.

2.2. Metallic glass matrix composites (MGMC)

BMGs found a wide range of application in the mid-1990s due to the rush in commercial market to find the suitable material with better properties and low cost of manufacture. But, it was found that there are some of the faults associated with these alloys like low fracture toughness, low ductility at room temperature. So, research work started in early 2000s to find better alternative to these materials with improved toughness. It was found that brittle character of BMGs can be lessened with addition of some crystalline phases in the matrix phase of BMG. This led the researchers to investigate the centimeter or greater thickness BMG matrix composites (BMGMCs) for structural (load bearing) applications. High-strength, hardness and toughness of BMGMCs make them fit for high-performance load-bearing applications, such as spacecraft shielding and panels for military vehicles [26]. The first toughened in situ BMGMC were developed by Hays and Kim at Caltech in 1999 by recognizing that a beta stabilizer, Nb added to matrix phase could make the dendrite phase softer [27]. Zr-Be-based composites are the most desirable BMGMCs because of lack of any stable compound found between the Be and constituents which can prevent heterogeneous nucleation actuated by dendrites during quenching. BMGMCs are finding a wide application in fields of aerospace, defense, sports etc. Some of them are like spacecraft debris shielding, golf club, energy absorbing cellular structures, gear, car door panels, armor and penetrators [26].

2.3. Formation of glassy state in metals

A liquid can form a glass if and only if its actual cooling rate is higher than the critical cooling rate (R_c). The transition occurs at a temperature known as glass transition temperature (T_g), when molten metal is under-cooled at the critical cooling rate so as to suppress the nucleation and crystal growth. This is the reason why the first metallic glass (~10μm thickness) was formed at a very high cooling rate of about 10^5-10^6 s^{-1} [28, 29]. The glass-liquid transition is the reversible transition from a relatively hard and brittle state into a molten or rubber like state below the melting temperature of metal (Fig. 2.2). Glass transition

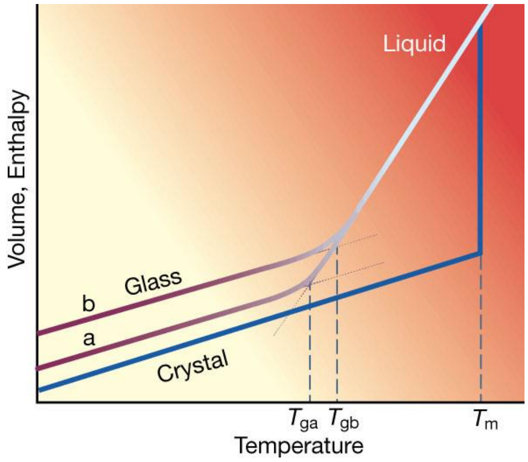

Fig. 2.2. Volume change associated with heating and cooling in systems susceptible to glass formation [30]

temperature increases with increase of cooling rate and the dimension of glass decreases as shown in curve 2.2b for glass having glass transition temperature, $T_{gb} > T_{ga}$. Metallic glass or amorphous metals are termed when the glassy state is formed with a metallic melt under-cooled below the T_g value. It becomes easy for the combination of two or more atoms of metals whose atoms differ in size greatly to form glassy state as crystallization process becomes difficult [29].

2.4. Glass forming ability

The glass forming ability (GFA) of a melt mainly depends on the critical cooling rate (R_c) for glass formation. It is the minimum cooling rate required so as to keep the melt amorphous without precipitation of any crystal during solidification. The smaller the R_c, higher the GFA of a system should be [31]. The most extensively used criteria of GFA to reduce R_c value are (i) The reduced glass transition temperature T_{rg} (glass transition temperature T_g over liquidus temperature T_l, i.e.,T_g/T_l), an alloy should have a high reduced glass transition temperature which increases the viscosity of melt, thus enhances GFA ($0.4< T_{rg}<0.7$). This judges only the condition under which glass is formed and doesn’t address the stability. (ii) The super cooled liquid region ΔT_{xg} (the difference of temperature between the onset of crystallization temperature, T_x and the glass transition temperature, T_g), thermal stability in metallic glass is usually evaluated by determining the temperature difference ΔT_{xg} upon heating at a constant rate. For some systems, it has been verified that larger values of ΔT_{xg} tend to be coupled with lower values of critical cooling rate (R_c), signifying that glassy phase is very stable. (iii) Lu and Liu argued that the GFA of an alloy should comprise the criteria for both glass formation and its stability. Thus, both T_{rg} and ΔT_{xg} are combined into one criterion. Thus a new parameter γ was defined as:

$$\gamma = \frac{T_x}{T_g + T_l} \text{ -- } (2.1)$$

This parameter was found most appropriate to explain GFA of metallic glasses ($0.350 < \gamma < 0.500$) [31]. Later Inoue [32] has formulated three practical rule for achieving high GFA (a) The alloy system should contain at least 3 components (b) The atomic size disparity between ingredient elements must be at least 12%, it makes crystallization more difficult and can be prevented in many instances by extremely rapid cooling of the melt (c) there should be a high negative heat of mixing between the alloying elements as positive heat of mixing may lead to phase separation so that the elements may not alloy together.

2.5. Different types of metallic glass

Metallic glasses can be classified into two categories viz. (i) metal-metal type (ii) metal-metalloid type. Distinctive constituent elements of BMGs can be grouped as: alkaline earth metals (Mg, Ca), simple metals (Al, Ga) in IIIA and IVA groups neighbouring the semiconductors, transition metals including early transition metals (Ti, Zr, Mo, Cr, Nb etc.) and late transition metals (Fe, Co, Ni, Pd, Cu etc.), rare earth metals (La, Ce, Nd), and non-metals (B, C, P, Si). Almost all MGs comprise elements from at least two groups and so there are certain sample pairs upon which even more complex BMGs are based [28].

The metal-metalloid BMGs comprise mainly early transition metals or late transition metals combined with non-metals. A few examples of such BMGs are Ni–P, Fe-B, Co-B, Pd–Ni–Cu–P, Fe–Cr–Mo–P–C–B. The metal-metal amorphous alloy system consists of only the metals. Some examples of such type of alloys are Fe-Nd-Al, Ni-Nb-Ti, Cu-Zr-Ti [28, 33].

2.6. Structure of metallic glasses/amorphous metals

Amorphous is the word employed to structure with absence of crystalline structure or having short range order arrangement of atoms. Metals exhibit different physical and mechanical properties due to the crystal structure and presence of defects in it. Metallic glasses have not clearly defined atomic structure and associated defects within. So, it becomes difficult to understand the origin of their properties. Spaepen [15] proposed the free volume model to describe the deformation mechanism occurring in metallic glasses. However, an important question in structure study of these glasses was whether the arrangement of atoms is in random fashion or a local ordering exists there. Structural arrangement of atoms can be obtained by diffraction method, calorimetry, viscosity measurement and other techniques. The calorimetry method leads to two different approach namely direct and indirect method of analysis [34]. In the direct method of investigation the consistent diffraction data is treated by Fourier transform methods from which radial distribution function (RDF) is evolved. Investigation of the RDF gives the average inter-atomic spacing and the near-neighbour co-ordinations in the glass. The indirect method comprise of generating a structural model for glass and calculating the intensity function or the RDF and comparing it with experimental intensity. Fig. 2.3 shows the schematic sketches of the atomic arrangements and its pair distribution function in a gas, liquid, glass and crystal.

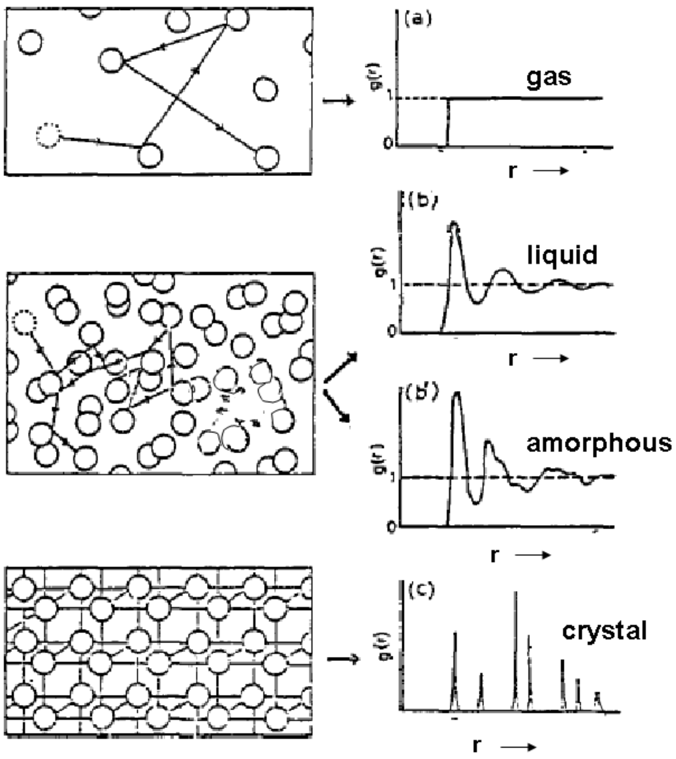

Figure 2.3. Schematic to represent the atomic configuration and radial distribution function of crystalline, liquid and amorphous structures [35].

2.7. Processing routes of glass formation

2.7.1. Methods of metallic glass synthesis (Rapid solidification processing)

Duwez and co-workers showed that the nucleation and crystal growth can be bypassed in certain melt alloys to obtain amorphous metals [2]. Some of the materials were developed during the second half of twentieth century so as to fulfil the combination of better properties together with performance. Different types of non-equilibrium processing techniques used for the synthesis were rapid solidification processing (RSP), plasma processing, vapour deposition, irradiation, and spray deposition. Some other methods not involving any quenching are mechanical alloying, electro-deposition of alloys etc [36–38].

The basis of these techniques were ‘to energise and quench’ the material and synthesize the metastable phase [36]. Energizing of crystalline material involves the change state change from solid to liquid state. Materials are first melted and then vaporized during vapour deposition in case of RSP. Then this energized material is ‘quenched’ by rapid solidification processing to obtain a highly metastable phase of the material. These metastable phases can be further transformed to less metastable state by some annealing methods so as to obtain the desired microstructure and properties.

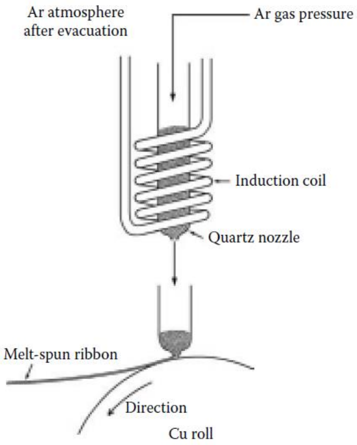

Figure 2.4. Schematic of a melt spinning process [39]

To obtain uniformity of cross-section and high solidification rate some techniques were developed for RSP. Melt spinning is one of them to obtain amorphous ribbons, wires, and filaments. The alloy is melted in a crucible and then ejected through an orifice and solidified against a fast rotating copper chill. As the solidification starts the ribbon is expelled from the chill surface or heat sink. The solidification rate achieved in this method is about 10^5-10^6 K s^{-1}. Typical size of the ribbons produced are 2-5 mm in width and 20-50 μm in thickness. The schematic of melt spinning is shown in Fig. 2.4 [39].

2.7.2. Methods of bulk metallic glass synthesis

A number of procedures have been suggested to manufacture BMGs since its development. Some of them are like water quenching method, high pressure die casting, mechanical alloying etc.

2.7.2.1. Water quenching method

Alloys are made by melting in an arc furnace or by induction melting. The alloy is placed in a quartz tube with a flux (oxide like B_2O_3 to remove impurities and improve GFA of alloy) and heated to its liquidus temperature so as to melt it completely. The melt is put in a quartz tube and quenched in agitated water. The cooling rate attained is roughly 10^2 K s^{-1}. A distinct feature of water quenching method is less residual stress in cast alloy formed due to slow cooling rate [39, 40].

2.7.2.2. High pressure die casting

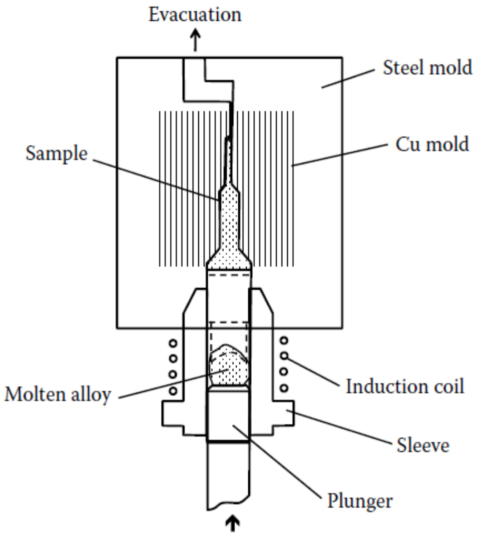

Figure 2.5. Schematic of a high pressure die casting [41]

Die casting method permits a high solidification rate so as to produce more complex shapes. The alloy is melted in a sleeve under Argon atmosphere with a high frequency induction coil. Melt formed is then moved into copper mould through a plunger by hydraulic pressure. As the melt comes in contact with mold it solidifies. The whole apparatus is emptied to avoid any gas entrapment and to give a pore free casting. Fig. 2.5 shows the schematic of a die-casting apparatus designed and used by Inoue et al. [41].

2.7.3. Mechanical alloying

A big difference between the mechanical alloying (MA) and procedures described up to now is that in earlier techniques, the alloy is prepared (monolithic or composite) in a single step

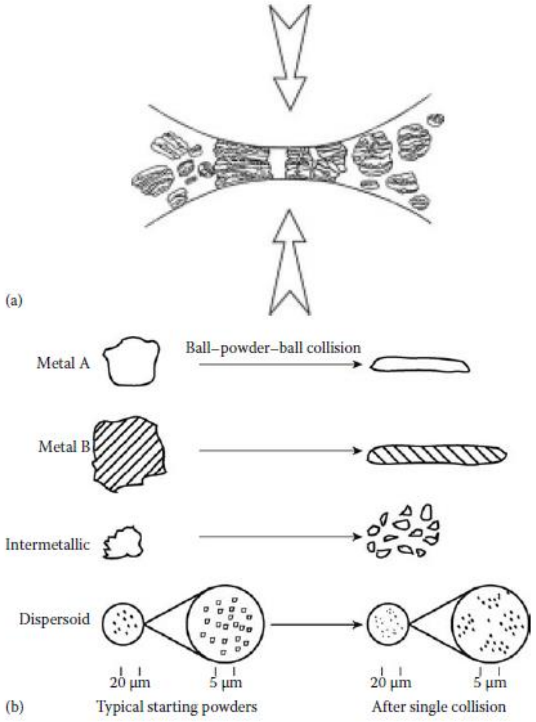

Figure 2.6. (a) Ball–powder–ball collision of powder mixture during MA and (b) deformation characteristics of representative constituents of starting powders in MA. [42]

whereas in MA powders of constituent elements are prepared and then consolidated to form a single bulk amorphous alloy through application of pressure or heat. The powder blend is made of different elements and placed in a milling container under inert atmosphere along with the grinding medium i.e., spherical balls made of stainless steel, tungsten carbide. The container is then placed inside mill and whole mass is agitated violently for desired time length. The powder particles entrapped between two balls go through a process similar to rolling and is subjected to compressive, shear or impact forces depending on the type of milling. Particles get fragmented into smaller particles by abrading if brittle and flattened into pancake shape if it is soft. [42].

Table 2.1. Glassy alloy system with calendar year, cooling rate and size [1, 32]

Year	Alloy system	Technique	Cooling rate ($K\ s^{-1}$)	Shape /thickness/diameter
1959	Cu-Ag	Gun technique	10^6	Thin foil/40μm
1971	$Pd_{80}Si_{20}$	Melt spinning	10^5-10^6	30 cm length ribbon
1988	Mg-Ln-M	Copper mold casting	10^3-10^{-1}	25mm dia. rod
1990	Zr-Al-Cu	Tilt casting	10^3-10^{-1}	15mm dia. rod
1993	Ti-Zr-(Fe, Co, Ni)	Suction casting	10^3-10^{-1}	10 mm dia. rod
1995	Zr-(Ti, Nb, Pd)-Al-(Fe, Cu, Ni, Cu)	Suction casting	10^3-10^{-1}	30 mm dia. rod
2001	Cu-(Zr, Hf)-Ti, Al, Ag	Copper mold casting	10^3-10^{-1}	10-25 mm dia. rod
2004	Ni, Pd, P	Water quenching	10^3-10^{-1}	15 mm dia. rod
2006	Co-(Cr, Mo)-(C,B)-(Y, Er)-(Fe, Co, Ni, Cu)	Copper mold casting	10^3-10^{-1}	10 mm dia. rod

Table 2.1 shows the different glassy alloy systems with their preparation technique and year of manufacture.

2.8. Application of metallic glasses

Metallic glasses are finding a wide range of application in various fields such as automobiles, electronic gadgets, sporting equipments, magnetic core, jewellery etc. which are listed below with properties in Table 2.2.

Table 2.2. BMG alloy system and their applications [10, 43, 44]

Base alloy	Property	Application	Alloy system
Zr based	Smaller size, high sensitivity, high pressure endurance	Diaphragm used in pressure sensors in automobile inds.	Zr–Al–Ni–Cu
	high torque	micro geared motors used in cell phones	
	`High elastic energy	Sporting equipment	Zr-Ti-Cu-Ni-Be
Ti based	High tensile strength, large elastic elongation, high corrosion resistance	Glassy alloy pipes used in coriolis flow meter	Ti–Zr–Cu–Ni–Sn
Fe based	Low core loss, high electrical resistivity	Magnetic core	Fe–Cr–P–C–B–Si
Pt and Pd based	High hardness, wear and corrosion resistant, lustre,	Jewellery	
Pt based	High fracture toughness	Die material	Pd-Cu-Ni-P

2.9. Deformation behaviour of metallic glasses

Metallic glasses have high tensile strength but have very less ductility and fails just after the yield point is reached. The deformation behaviour of metallic glasses may be classified as (a) inhomogeneous deformation and (b) homogeneous deformation.

2.9.1. Inhomogeneous deformation

The deformation occurring at low temperature, high stress condition is inhomogeneous. At temperature lower than $0.5T_g$ deformation is localized in few very thin shear bands that are formed on planes of maximum resolved shear stress. The material fails catastrophically as the deformation is unstable at high stress. Metallic glasses undergo strain softening at low stress and high strain rates which leads to the creation of shear bands. These shear bands lead to decrease in local viscosity of glass. This phenomenon is described by the creation of free volume due to flow distension, structural order creation by shear transformation zone (STZ) operation, local heating [39]. Two possible reasons were suggested for the inhomogeneous deformation through shear band formation. These are:

(i) Decrease in viscosity due to formation of more free volume with deformation. This causes decrease in density of glass and so resistance to deformation. Spaepen derived an expression for steady state inhomogeneous deformation in metallic glasses on the basis of competition between creation and diffusional annihilation of free volume [15].

(ii) Adiabatic heating occurs in local region of shear band and so lead to viscosity fall of the metallic glass [45].

The ‘pop in’ events in load-displacement curves of nano-indentation are associated with activation of shear bands. In case of slow indentation rate a single shear band is able to accommodate deformation. When the strain rate is increased atoms do not get enough time to accommodate deformation and so multiple shear bands are formed resulting in a smooth load-displacement curve [11].

2.9.2. Homogeneous deformation

The deformation occurring at high temperature and low stresses is homogeneous. Such condition leads to Newtonian flow and thus strain rate is proportional to stress. But with increase of stress value applied strain rate sensitivity decreases and flow become non-Newtonian. At high temperature greater than $0.8T_g$ glass have viscous flow in which plastic strain is distributed continuously, but not inevitably equally between different volume elements of glasses [46]. It causes significant plastic flow and therefore is of commercial importance. The homogeneous deformation behaviour can also be explained on the basis of STZ as proposed by Argon [14]. A changeover from Newtonian to non-Newtonian deformation behaviour is associated with crystallization (formation and precipitation of nano-crystals) within the glassy matrix at high temperature. It is also investigated that homogeneous deformation is associated with crystallization of glass partially [39].

2.9.3. Deformation maps

A steady state constitutive flow law describes different modes of deformation using equation

$$\dot{\gamma} = f(\tau, T, structure) \text{ -- } (2.2)$$

where, $\dot{\gamma}$ is strain rate, τ is the shear stress and T is temperature. *'structure'* represents all the structural parameter of the material

The steady state condition means that all the structural parameters are determined by some external parameters-temperature and stress. Spaepen [15] introduced a deformation map for metallic glasses based on the above concept. He calculated boundary between homogeneous and inhomogeneous deformation regions. Fig. 2.7 shows the deformation map of metallic glass to indicate various modes of deformation. Stress is plotted on Y-axis on a logarithmic scale and temperature on X-axis. Map shows that homogeneous deformation occurs at low stress and high temperature and shows high strain rate dependency which are indicated by strain rate contours. On the other hand in high stress levels and low temperature region, inhomogeneous deformation takes place and is independent of strain rate applied. Unlike melt spun metallic glass ribbon, BMGs have wide super-cooled liquid region, ΔT_x (T_x-T_g). Here T_x is crystallization temperature and T_g is glass transition temperature for glass [39].

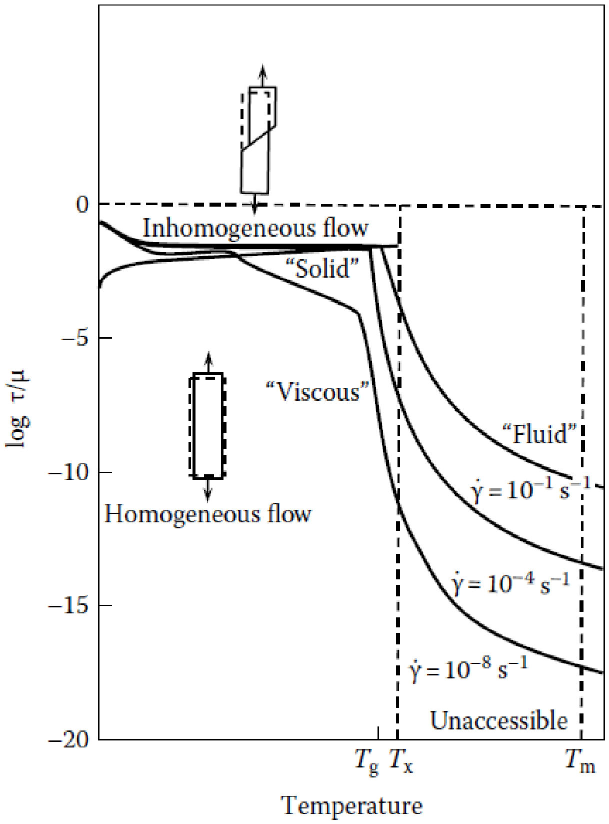

Figure 2.7. Deformation map for metallic glass proposed by Spaepen [15]

2.10. Mechanical properties determination through nano-indentation

When an indenter is inserted in a sample both elastic and plastic deformation occurs, and results in a hardness impression. During unloading only the elastic portion of deformation is recovered and so it provides only the elastic solution in modelling the contact process (Fig. 2.8). In nano-indentation experiments load applied on the indenter and depth of indentation are continuously measured for the desired indentation depth. The data for the loading and unloading of indenter are plotted on load-displacement (*P*-*h*) plot to obtain some of the elasto-plastic properties of a sample such as hardness of the alloy, stiffness calculated by slope of unloading curve, elastic modulus (*E*), Yield strength (σ_y), residual stress etc.

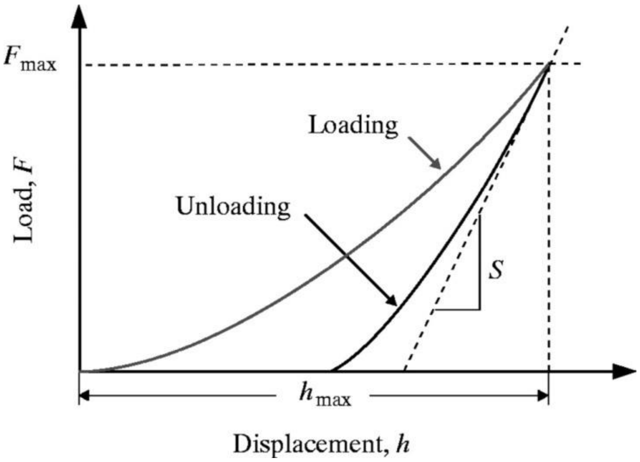

Figure 2.8. Load-Displacement curve with key parameters, F_{max}, peak indentation load; h_{max}, indenter displacement at peak load; S, contact stiffness [47]

The stiffness (*S*) calculation is made through the slope of unloading curve at maximum loading point (dF/dh). The expression for the stiffness is given below [48].

$$S = \frac{dF}{dh} = \frac{2}{\sqrt{\pi}} E^* \sqrt{A_c} \text{ --- } (2.3)$$

where, A_c = Projected area of elastic contact

$$\frac{1}{E^*} = \frac{1-\nu^2}{E} + \frac{1-\nu_i^2}{E_i} \quad \text{--} \quad (2.4)$$

E^* describes the reduced elastic modulus, and it consists of elastic modulus of indenter, E_i and its poison's ratio, v_i. *E and v* represents the elastic modulus and poison's ratio respectively of specimen [48]. The equation (2.3) for stiffness calculation hold good equally for spherical, cylindrical and other type of indenters as well.

There occurs elastic deformation only during indentation initially which can be described by Hertz's theory and expression for force *(F)* can be given by

$$F = \frac{4}{3} r^{1/2} E^* h^{3/2} \quad \text{--} \quad (2.5)$$

r, is the radius of indenter, h is the indentation depth and E^* is reduced elastic modulus.

Hardness (*H*) of the material is the mean pressure the material supports under the load. So *H* can be calculated as,

$$H = \frac{F}{A_c} \quad \text{---} \quad (2.6)$$

$$A_c = \frac{\pi d_c^2}{4} (r^2 = d_c^2 + h_c^2) \quad \text{---} \quad (2.7)$$

$$h_c = h - \varepsilon \frac{F}{S} \quad \text{--} \quad (2.8)$$

where, *F* is force on indenter, A_c is area of contact, *h* is depth of indentation. h_c (Eq. 2.8) is employed to determine the projected area of contact by Sneddon's equation [49]. ε is geometric constant which is 0.75 for spherical indenters. d_c is diameter of residual impression in surface. S is contact stiffness [50].

2.11. Effect of state of stress

Table 2.3. Mechanical properties of metallic glasses in compression, tension deformation studies

Composition (at.%)	$\sigma_{c,f}$ (MPa)	σ_y (MPa)	ε_f (%)	H_v	D_c (mm)	Fracture features	Reference
$Cu_{45}Zr_{47.5}Ag_{7.5}$	1820		2.9	556	6.0	Shear bands at 45° to the loading direction	[51]
$Cu_{45}Zr_{45}Ag_{10}$	1810		0.3	542	6.0		
$Cu_{42.5}Zr_{47.5}Ag_{10}$	1780		0.3	534	5.0		
$Cu_{45}Zr_{50}Ag_{5}$	1885		0.2	585	3.0		
$Cu_{47.5}Zr_{47.5}Al_{5}$	2265	1547	18		2.0	Wavy shear bands	[52]
$Cu_{46}Zr_{46}Al_{8}$	2050	1200	2.9		2-5		[53]
$Zr_{55}Al_{20}Co_{20}Cu_{5}$	2200		2.7		3-5	Vein pattern	[54]
$Ti_{40}Zr_{25}Ni_{8}Cu_{9}Be_{18}$		1720	0.034		3	Shear bands at 39.5˚to loading direction	[55]

Table 2.4. Mechanical properties of metallic glass under indentation experiment

Alloy	Sample dimension	Load (N)	Hardness (GPa)	σ_y (Gpa)	Indenter	Reference
Zr–5Ti–17.9Cu–14.6Ni–10Al (wt.%) (vit.105)	1.6mm × 5mm × 30 mm	160	5.5	1.96	Spherical (*Φ* 400μm)	[56]
$Zr_{40}Ti_{14}Ni_{10}Cu_{12}Be_{24}$	4mm×2mm×2mm		5.4	2.3	Berkovich	[57]
$Zr_{55}Cu_{30}Al_{10}Ni_{5}$	*Φ* 2mm ×1mm	0.004 -0.5	8-6.5		Berkovich	[58]
	Φ 2mm×100mm	1	5		Vicker's	
$Pd_{42}Ni_{40}P_{18}$	*Φ* 5mm	4.9-49	5.8-6		Vicker's	[59]
$Zr_{52.5}Al_{10}Ti_{5}Cu_{17.9}Ni_{14.6}$	0.6 mm × 3 mm × 15.3 mm		6.64	1.65		[60]

Table 2.5. Mechanical properties of Zr-based glass matrix composites in compression and tensile deformation

Composition (at.%)	Crystallite phase	σ_y (GPa)	ε_f (%)	E (GPa)	H (GPa)	Dim. (mm)	Fracture features	References
$Zr_{55}Al_{10}Cu_{30}Ni_5$	(17.5% Tungsten)	2 (compressive)			6.1±0.2	*Φ* 3×6		[61]
$Zr_{36.6}Ti_{31.4}Nb_7Cu_{5.9}Be_{19.1}$	42%,51%,67% of respectively BCC dendrites of Zr, Ti, Nb	1.4(tensile)	9.58	84.3	-	*Φ* 3-3.05	Shear bands at 45º to the principal axial loading direction	[9]
$Zr_{38.3}Ti_{32.9}Nb_{7.3}Cu_{6.2}Be_{15.3}$		1.3(tensile)	10.8	79.2				
$Zr_{39.6}Ti_{33.9}Nb_{7.6}Cu_{6.4}Be_{12.5}$		1.1 (tensile)	13.1	75.3				
$Zr_{57}Al_5Nb_{10}Cu_{15.4}Ni_{12.6}$	10% W	1.9 (compressive)	7	96	-	*Φ* 3×6	Shear bands at 45° to the principal axial loading direction	[6]
$Zr_{57}Al_5Nb_{10}Cu_{15.4}Ni_{12.6}$	10% Ta	1.8 (compressive)	3	87.5	-			
$Zr_{57}Al_5Nb_{10}Cu_{15.4}Ni_{12.6}$	10% SiC	1.0 (tensile)	5	71				

Table 2.6. Mechanical properties of MGs and GMCs obtained under different modes of deformation (compressive, tensile, shear and indentation) by simulation studies

BMGs	$(CuZr)_{98}Al_2$ [62]	$Zr_{47}Cu_{31}Al_{13}Ni_9$ [63]	$Cu_{64}Zr_{36}$ [64]	$Cu_{57}Zr_{43}$ [18]	$Cu_{65}Zr_{35}$ [19]
Dimension/ atoms	$320\times320\times120$ Å^3	$160\times160\times$ 124 Å3/200000	5.5×10^5 atoms	$32.4\times32.4\times$ 32.4 Å/2000	3200
Potential	TB-SMA	TB-SMA	EAM	LJ	EAM
Strain rate (s^{-1})	8.3×10^8	1.37×10^9	4×10^7		5×10^7
Yield strength (MPa)	-	-	2400	2100	3500
Hardness (GPa)	5.5 (approx.) at 48 Å	6.5(approx) at 40 Å	-	-	-
Young modulus (GPa)	85	-	53.33	33.3	58.3
Maximum load (nN)	-	300	-	-	-
Type of load	Indentation	Indentation	Tensile	shear	compression

2.12. Additional details about Zr-Cu based metallic glasses

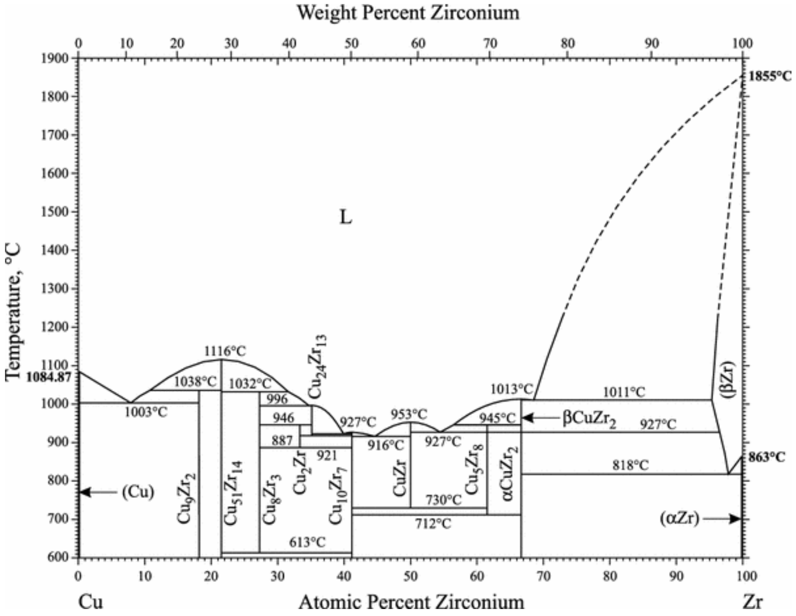

Figure 2.9. Cu-Zr phase diagram [65]

Fig. 2.9 shows the schematic phase diagram of Cu-Zr based metallic glass [65] which is a useful tool in selecting the alloy with good glass forming ability. The melting point of $Cu_{50}Zr_{50}$ alloy can be seen to be depicted as 953 ° C (1226 K). The EAM potential used for simulation of quenching and indentation in the present study is validated by using the above value of melting point. The validation is done by melting simulation and radial distribution function analysis (RDF) is done to confirm the melting point of the Zr-Cu and Zr-Cu-Al model. The procedure is described in detail in result and discussion chapter of this thesis.

2.13. Gaps in the literature (classical molecular dynamics simulation studies)

Extensive experimental studies have been carried out to understand the deformation behaviour of Zr- based MGs and Zr-based MGMCs.

- However there are seldom studies reported on the influence of volume fraction of crystalline phase on the deformation behaviour.

Extensive studies using classical molecular dynamics (MD) have been carried out to understand the stress-strain characteristics and atomistic mechanism of plastic deformation in Cu-Zr based metallic glasses.

- There are seldom atomistic simulation deformation studies reported on the Zr-based MGs and GMCs.
- The effect of strain rate and temperature on the load-displacement characteristics in Zr-based MGs and GMCs during nano-indentation are seldom reported.
- Phase transformation during deformation is not reported.
- The influence of crystallite shape, volume fraction, distribution on the mechanical properties and load-displacement characteristics during nano-indentation.

2.14. Broad aims and objectives

a) To investigate the effect of strain rate (10^9 s^{-1}-10^{11} s^{-1}) and temperature (100 K, 300 K and 500 K) on the load-displacement behaviour and the response on the mechanical properties of $Zr_{50}Cu_{50}$ based MG and GMCs during nano-indentaion.

b) To study the effect of crystallite volume fraction on the load-displacement behavior.

c) To analyze the structural changes taking place during nano-indentation by CSP values.

d) To investigate the effect of alloying element (Al) on the load-displacement behaviour and on the mechanical properties.

e) To study the effect of crystallite distribution (single-spherical and multi-spherical) and shape (spherical and cylindrical) on the load-displacement response.

CHAPTER 3

MOLECULAR DYNAMICS SIMULATION PROCEDURE

3. Different simulation techniques

We carry out computer simulations in the hope of understanding the properties of assemblies of molecules in terms of their structure and the microscopic interactions between them. This serves as a complement to conventional experiments, enabling us to learn something new, something that cannot be found out in other ways [66]. In order to gain control over properties of and processes in materials, an atomic scale understanding is of primary importance. To this end two main techniques are commonly used viz. Molecular Dynamics (MD) and Monte Carlo (MC) [67].

3.1. Introduction to classical molecular dynamics

Classical molecular dynamics (MD) is a simulation tool used to understand the property of assemblies of molecules in terms of their structure and the microscopic interactions between them. It allows one to gain insight into situations that are impossible to study experimentally such as extreme temperature and pressure conditions. In MD simulations atoms and molecules are supposed to follow the Newtonian dynamics and have “force field” present between them for interaction to occur. MD simulation is often used in the study of biomolecules and proteins and also in material science. MD was introduced for the first time in 1957 [68] and 500 hard spheres were simulated and studied. Further, some 864 atoms were studied with motion of individual atoms in liquid Argon [69]. But after the invention of Teraflop parallel simulating system using massively parallel computers about 10^9 atoms were simulated together [70]. The workload is distributed among various processors of parallel computers which increases the calculation. Most time consuming task during simulation is the calculation of potential (force field) as a function of coordinates of atoms. Another factor which affect the time taken by CPU evaluation is the size of integration time-step i.e., time length between evaluation of potential. Time-step chosen in MD calculation should be small so as to avoid discretization errors (much smaller than the fastest vibrational frequency in the system). Typically it is of the order of 1 femtosecond (10^{-15}). Simulation and calculation between atoms is done only if potential between atoms are known or given as input to the computer.

3.1.1. Advantages:

a) It is based on the solution of the equations of motion for all particles in the system.

b) Complete information on atomic trajectories can be obtained, but time of the simulations is limited (up to nanoseconds).

c) The main strengths of the MD method is the ability to study fast non-equilibrium processes with atomic-level resolution (e.g. microscopic mechanisms of damage/plastic deformation due to a shock wave propagation, dynamic fracture and crack growth, ion bombardment, cluster impact, etc.).

d) The only input in the model – description of interatomic/intermolecular interaction

3.1.2. Limitations:

a) With MD we can only reproduce the dynamics of the system for ≤ 100 ns. Slow thermally activated processes, such as diffusion, cannot be modelled.

b) Potentials are available for only few metallic systems.

c) Electrons are not present explicitly; they are introduced through the potential energy surface that is a function of atomic positions only (Born-Oppenheimer approximation).

3.1.3. Inter-atomic potential

In MD, atoms interact with each other and forces act among them which changes along with the change of position of atoms. These forces (F_i) are calculated as gradient of potential energy function which is dependent on atom/particle coordinate as

$$F_i = \frac{-\partial U}{\partial r_i} \quad \text{---} \quad (3.1)$$

where, r_i is the position vector of an atom *i*. Potential energy, U is a function of atomic position and never changes with translation or rotation of atomic position. Equation (3.1) represents the law of conservation of mechanical energy $E=K+U$, where E is total energy, K is kinetic energy and U is potential energy.

3.1.4. Potential in MD simulation

Embedded atom method potential describes the energy between the two atoms present. The energy is sum of functions of separation between atoms and its neighbors. It was developed by Daw and Baskes (1984) [71] to study defects in metals. The total energy (E_{tot}) of an N-atom system is given by

$$E_{tot} = \sum_{i} F_i(\rho_i) + \frac{1}{2}\sum_{\substack{i,j \\ i \neq j}} \varphi_{i,j}(r_{i,j}) \quad \text{--------------------------------------- (3.2)}$$

where, $\varphi_{i,j}(r_{i,j})$ is a short range pair potential between atoms with separation $r_{i,j}$, $F_i(\rho_i)$ is the embedding energy of atom i with electron density ρ_i due to all its neighbours is expressed below:

$$\rho_i = \sum_{j \neq i} f_j(r_{ij}) \quad \text{-- (3.3)}$$

The other type of potentials are L-J potential [72], Empirical potential [73].

3.1.5. Simulation method in molecular dynamics

In MD atomic/molecular motion obeys the law of classical mechanics. Set of initial position and velocities of various atoms are given and subsequent time evolution is determined. The result shows how position and velocities of atoms are changing with time. The differential equation embodied in Newton's second law (Force = mass × acceleration) is solved for obtaining the trajectory of atoms.

$$\frac{\partial^2 x}{\partial t^2} = \frac{F_{xi}}{m_i} \quad \text{-- (3.4)}$$

The above equation describes the motion of particle of mass m_i along one coordinate (x_i) with F_{xi} being the net force on particle in the same direction.

3.1.6. General steps of molecular dynamics simulation

a) Initial position and velocity is assigned to every atom.

b) Force on all the atoms are computed with inter-atomic potential known.

c) Newton's equation of motion is integrated to obtain trajectory of atoms. They are repeated again and again until desired property of all the atoms of system is obtained.

3.1.6.1. Initializing positions and velocity of atoms

Initial position of all atoms is determined either by lattice structure and composition or by random method. This depends on whether the system to be simulated is crystalline or amorphous. These positions can also be assigned from earlier simulation results. Initial velocity is found from the temperature of the system and calculated from random distribution given by statistical mechanics. Systems containing small number of atoms, their linear momentum are scaled to zero because the random assignment of velocity may not sum to zero exactly. Velocities can also be assigned from previous simulation results.

3.1.6.2. Force calculation

Force calculation on each atom is the most time consuming part in MD simulation. The force on atom 'i' due to the other atoms 'j' surrounding it is calculated from the inter-atomic potential which exist between each pair of atom and controls interaction among them. If $U(dij)$ is the interaction potential between any pair of atom 'i' and 'j',the force on atom 'i' due to atom 'j' is given by

$$\vec{F}_{ij} = \frac{(\vec{r}_i - \vec{r}_j)}{\left|\vec{r}_i - \vec{r}_j\right|}\left(-\frac{\partial U(d_{ij})}{\partial d_{ij}}\right) \text{--} (3.5)$$

where, r_i and r_j are position vectors of atoms '*i*' and '*j*' and d_{ij} is distance between them and is given by

$$d_{ij} = \left|\vec{r}_i - \vec{r}_j\right| \text{--} (3.6)$$

In the present simulation studies EAM-FS potential is used for binary Cu-Zr system developed by Mendeleev [74]. In Finnis/Sinclair model [75] total energy of an atom is represented by

$$E_i = F_\alpha\left(\sum_{j\neq i}\rho_{\alpha,\beta}(r_{i,j})\right) + \frac{1}{2}\sum_{j\neq i}\varphi_{\alpha,\beta}(r_{i,j}) \text{----------------------------------} (3.7)$$

where, F is the embedding energy which is a function of ρ, φ is a pair potential interaction, ρ is the electron density which is a functional specific to the atomic types of both atoms i and j so that different elements can contribute differently to the total electron density at an atomic site depending on the identity of the element at that atomic site and alpha and beta are the element types of atom i and j.

3.1.6.3. Integrating the equation of motion

As the force on the atoms is calculated, the next step is to integrate Newton's equation of motion. There are several algorithms and Velocity-Verlet is one of the well-known algorithms which calculates the position and velocity of atoms after time Δt from the known values at time t, which is based on following equation

$$x(t+\Delta t)=x(t)+v_x(t)\Delta t+\frac{1}{2}a_x(t)(\Delta t)^2 \tag{3.8}$$

$$v_x(t+\Delta t)=v_x(t)+\frac{a_x(t)+a_x(t+\Delta t)}{2}\Delta t \tag{3.9}$$

where $x(t)$, $v_x(t)$, $a_x(t)$ are x-component of position, velocity and acceleration of an atom at time t, respectively. $x(t+\Delta t)$, $v_x(t+\Delta t)$,$a_x(t+\Delta t)$ are x-component of position, velocity and acceleration of an atom at time $t+\Delta t$. The flow chart (Fig. 3.1) represents the scheme of this algorithm.

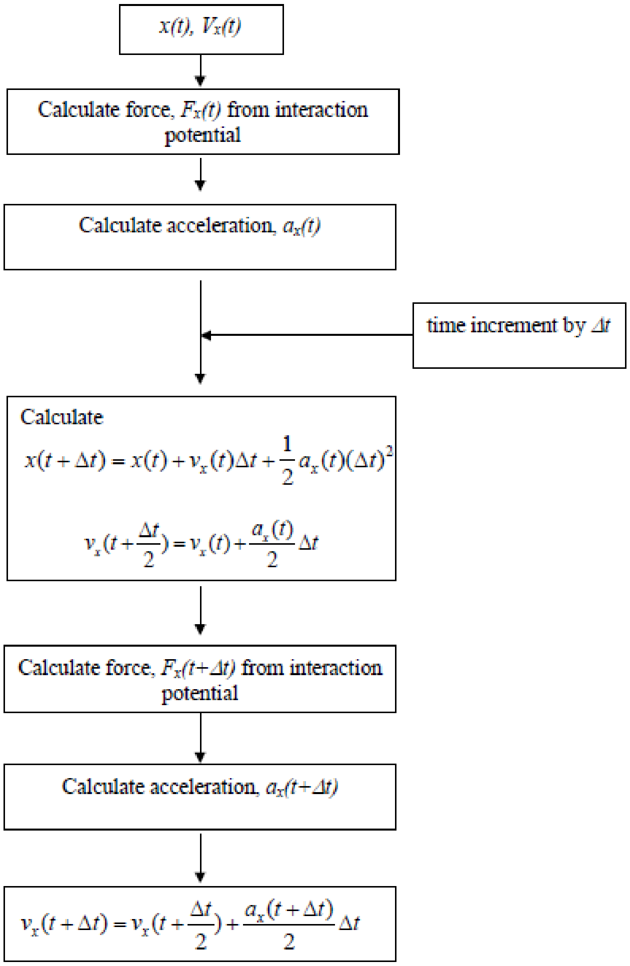

Figure 3.1. Flow chart indicating the execution of velocity-Verlet algorithm.

3.1.7. Periodic boundary condition

Periodic boundary condition is employed to simulate an infinite amount of matter with a finite simulation box size. Atoms coming out from one boundary of simulation cell emerge back from the opposite boundary. Fig. 3.2 represents the schematic of a periodic boundary condition.

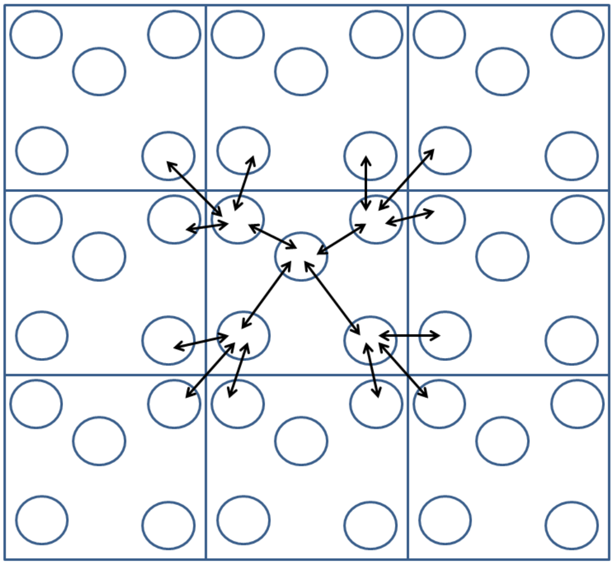

Figure 3.2. Schematic of a periodic boundary condition.

3.1.8. Ensembles

(a) NVE

In the microcanonical NVE ensemble the system is isolated from changes in atoms (N), volume (V) and energy (E). NVE integrator updates position and velocity for atoms in the group each time-step. There is no heat exchange with the surrounding. A trajectory of atoms is generated in the system and exchange of potential and kinetic energy occurs and the total energy remains conserved.

(b) NVT

In NVT ensemble the number of atoms (N), volume of the system (V) and the system temperature (T) remain independent variable and are constant during any process. Temperature is controlled by Noose-Hover thermostat.

(c) NPT

NPT is the isothermal-isobaric ensemble in which number of atoms (N), pressure (P) and temperature (T) are conserved. The volume of the system is allowed to change over time. Temperature and pressure are controlled by Nose-Hoover thermostat and Nose-Hoover barostat.

3.2. Monte Carlo method of simulation

Monte Carlo (MC) is a very general computational technique that can be used to carry out sampling of distributions. Random numbers are employed in the sampling, and often in other parts of the code. One definition of MC based on common usage in the literature is, any calculation that involves significant applications of random numbers [76].

3.2.1. Metropolis Monte Carlo (MMC)

3.2.1.1. Advantages

It generates random configurations with probability of each configuration defined by the desired distribution P (rN). This is accomplished by setting up a random walk through the configurational space with specially designed choice of probabilities of going from one state to another. Equilibrium properties can be found/studied (e.g. surface reconstruction and segregation, composition variations in the surface region due to the surface or substrate induced strains, stability of nanostructures). MMC is not limited to the calculation of equilibrium properties but can also be used to study dynamic properties [67].

3.2.1.2. Limitations

Atoms are displaced based on random numbers, thus in contrast with MD, MC technique is not deterministic [67].

3.2.2. Kinetic Monte Carlo (KMC)

3.2.2.1. Advantages

When the rate constants of all processes are known, we can perform KMC simulation in the time domain. Time increments are defined by the rates of all processes and are formulated so that they relate to the microscopic kinetics of the system. This method should be used when kinetics rather than equilibrium thermodynamics dominates the structural and/or compositional changes in the system.

3.2.2.2. Limitations

In contrast to MD, KMC is not self-consistent that is it must be assumed that is it must be assumed that all possible escape paths from the system’s current state can be found [67].

3.2.3. Kinetic Monte Carlo vs. Metropolis Monte Carlo

In MMC we decide whether to accept a move by considering the energy difference between the states, whereas in KMC methods we use rates that depend on the energy barrier between the states. The main advantage of kinetic Monte Carlo is that time is defined and only a small number of elementary reactions are considered, so the calculations are fast.

3.3. Advantages of MD over MC

a) MD simulations tend to be more efficient computationally than MC in the case where a system of atoms is being equilibrated at a new temperature or some other change in its conditions is implemented.

b) The advantage for MD results from the fact that the displacements of the atoms during an MD time-step are quite different from those discussed earlier for the MC methods. With classical MC, a displacement of a particle has nothing to do with the environment of the particle, but is chosen by random numbers along the three orthogonal co-ordinate axes.

c) Furthermore, coordinated moves of a number of particles such as those moving into a region of reduced pressure are not possible with Metropolis MC, whereas their presence in MD allows fast relaxation of a pressure pulse or recovery from artificial initial conditions [77].

d) MD simulation typically generates a single long trajectory of the system through phase space, MC typically samples configuration space.

3.4. Ab-initio molecular dynamics simulation technique

In a molecular-dynamics (MD) simulation the microscopic trajectory of each individual atom in the system is determined by integration of Newton's equations of motion. In classical MD, the system is considered composed of massive, point-like nuclei, with forces acting between them derived from empirical effective potentials. Ab initio MD maintains the same assumption of treating atomic nuclei as classical particles; however, the forces acting on them are considered quantum mechanical in nature, and are derived from an electronic-structure calculation [78]. Ab initio molecular dynamics (AIMD) revolutionized the field of realistic computer simulation of complex molecular systems and processes, including chemical reactions, by unifying molecular dynamics and electronic structure theory. Most of the Ab initio molecular dynamics simulations described in the literature have assumed that Newtonian dynamics was sufficient for the nuclei. While this is often justified, there are important cases where the quantum mechanical nature of the nuclei is crucial for even a qualitative understanding [79].

3.5. Introduction to LAMMPS (Large-scale Atomic/Molecular Massively Parallel Simulator)

3.5.1. Background

LAMMPS is a classical molecular dynamics simulation code run on parallel computers. It was developed at Sandia National Laboratories, US. It is a free source code which is distributed free of cost under the tem of GNU public license. The primary developers of this code were Steve Plimpton, Aidan Thompson and Paul Crozier [80].

3.5.2. General features

a) It runs on single or parallel processors

b) Optional libraries used: MPI and single-processor FFT

c) Distributed-memory message-passing parallelism (MPI)

d) Open source distribution

e) Easy to extend with new features and functionality

f) Syntax for defining and using variables and formulas

g) Run one or multiple simulations simultaneously (in parallel) from one script

3.5.3. Force fields

Some of the force fields that are employed in LAMMPS are:

a) pairwise potentials: Lennard-Jones, Buckhingam, Morse, Born-Mayer-Huggins, Yukawa,
b) soft, class 2 (COMPASS), hydrogen bond
c) charged pairwise potentials: Coulombic, point-dipole
d) manybody potentials: EAM, Finnis/Sinclair EAM, modified EAM (MEAM), embedded
e) ion method (EIM), ADP, Stillinger-Weber, Tersoff, REBO, AIREBO, ReaxFF, COMB
f) coarse-grained potentials: DPD, GayBerne, REsquared, colloidal, DLVO
g) water potentials: TIP3P, TIP4P, SPC

3.5.4. Ensembles, constraints, and boundary conditions

In LAMMPS ‘fix’ is any operation that is applied to the system during time-stepping or minimization. For example, the updating of atom positions and velocities due to time integration, controlling temperature, applying constraint forces to atoms, enforcing boundary conditions, and computing diagnostics etc. Fixes perform their operations at different stages of the time-step. If two or more fixes operate at the same stage of the time-step, they are invoked in the order they were specified in the input script.

a) 2d or 3d systems

b) Constant NVE, NVT, NPT, NPH, Parinello/Rahman integrators

c) thermostatting options for groups and geometric regions of atoms

d) pressure control via Nose/Hoover or Berendsen barostatting in 1 to 3 dimensions

e) simulation box deformation (tensile and shear)

3.5.4.1. Ensembles used in LAMMPS

In LAMMPS different ensemble used are NVE, NVT and NPT.

3.5.4.2. Boundary conditions

The boundary conditions that are employed in LAMMPS are:

i. p p p

ii. p p s

iii. p f p

where ‘p’ stands for periodic along the three directions, ‘f’ and ‘s’ stand for fixed and shrink wrapped, which are non-periodic.

3.5.5. Integrators

The integrators that are available in LAMMPS are:

i. velocity-Verlet integrator

ii. Brownian dynamics

iii. rigid body integration

iv. energy minimization via conjugate or steepest descent relaxation

3.5.6. Energy minimization

Atom coordinates are adjusted in LAMMPS so as to perform energy minimization. When one of the conditions of minimization criteria is satisfied, iterations are terminated. At that position system remain in local minimum potential energy state. The minimization algorithm is set by ‘min_style’ command.

3.5.7. Output

The output of LAMMPS simulation i.e., position and velocity of each atom is written on the dump file. It writes position and velocity of each and every atom dumped at an interval of time-steps. The values like temperature, pressure, potential energy of system at some particular number of iterations is written on the log file.

3.5.8. LAMMPS input script

LAMMPS simulation runs by reading the text file (in file). It reads one line at a time and as the whole program is read, it exits. Each command used causes LAMMPS to take action accordingly. LAMMPS input script consist of four parts:

(a) initialization

(b) atom definition

(c) settings

(d) run a simulation

(i) Initialization commands used in the present study

```
units          metal
boundary        p p p
atom_style      atomic
pair_style      eam/fs
read_data      abc.dat
```

(ii) Atom definition commands used in the present study

```
region         box block 0 1000 0 1000 0 0.85 units box
create_box     2 box
lattice        fcc 3.6151
```

(iv) Settings used in the present study

The next step after defining atoms is settting up force field coefficients, simulation parameters, output options etc.

```
pair_coeff        * * CuZr_mm.eam.fs Cu Zr (force field parameter)
minimize          1.0e-3 1.0e-6 100000 1000000 (energy minimization)
timestep          0.002
thermo            100 (output)
dump              1 all atom 1000 5050_q_2d_l_v.dump.lammpstrj (output)
log               log5050(quench_2d).data
```

(v) Run a simulation

MD simulation is run using the ‘run’ command.

3.6. OVITO (Open Visualization Tool) [81]

OVITO is visualization and analysis software used to understand atomistic simulation models. It is open source software freely available on internet. It is used to do cento-symmetry parameter analysis, common neighbour analysis coordination number analysis and radial distribution function. The model can be sliced to view the inner position of crystallites and effect of deformation on it [81].

3.7. HPC (High Performance Computing)

HPC is used to describe computing environment which utilize processing power of cluster of computers to address complex computational requirements, support application that require significant processing time or handle significant amount of data. All LAMMPS simulation codes were run on HPC with model no-HP DL360p. It is placed in data centre, computer centre, NIT Rourkela, Odisha.

3.8. Molecular dynamics (MD) simulation procedure to obtain $Zr_{50}Cu_{50}$ and $Zr_{50}Cu_{30}Al_{20}$ model MGs and GMCs

Samples of $Zr_{50}Cu_{50}$ and $Zr_{50}Cu_{30}Al_{20}$ based metallic glass and $Zr_{50}Cu_{50}$ based glass matrix composites containing 14 %, 30 %, 50 % crystallites (by volume) were prepared from crystalline structure (Fig. 3.3a and 3.3b) in a box of size 100 Å × 100 Å × 100 Å filled with 90,000 atoms (approximately) by simulated melting and quenching.

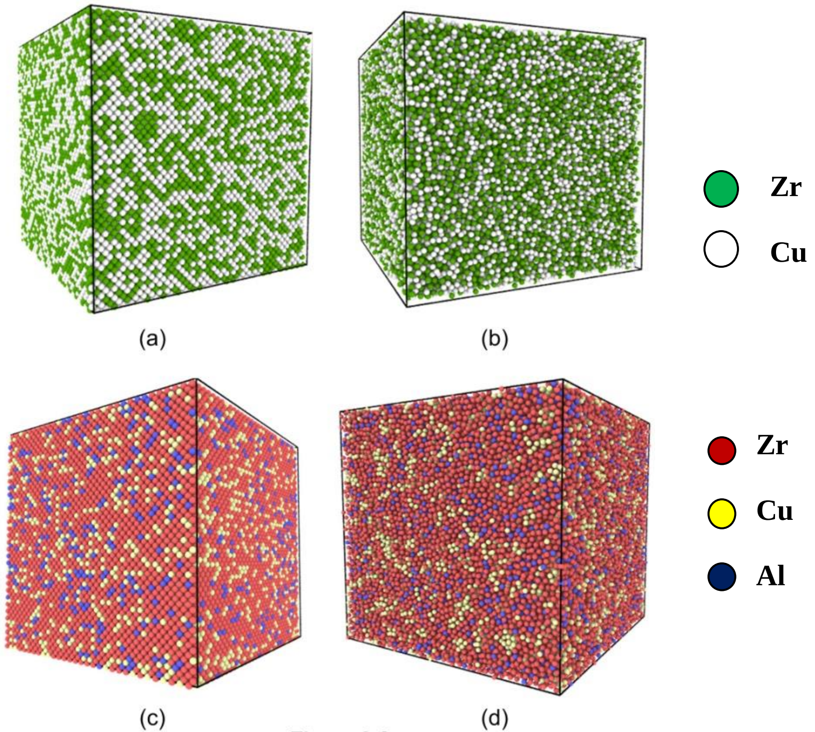

Figure 3.3

Figure 3.3. Atomic snapshot representing (a) crystalline $Zr_{50}Cu_{50}$ alloy (b) amorphous $Zr_{50}Cu_{50}$ alloy (c) crystalline $Zr_{50}Cu_{30}Al_{20}$ alloy (d) amorphous $Zr_{50}Cu_{30}Al_{20}$ alloy

The crystallites are group of ordered atoms having FCC crystal structure. The equilibration of model was done at minimum energy configuration at a temperature of 300 K. The samples were heated from 300 K to 2300K for 20 ps, allowing solid to melt and then held at 2300K for 100 ps. After that the samples were quenched from 2300K to 300K for 200 ps. Similarly, in the studies of Zhou et al. [82] Cu-Zr glass was obtained by quenching from a temperature of 2000 K. The pressure in the present study was maintained at 0 bar during whole process. Initially amorphous and composite samples were obtained by quenching at a cooling rate of 10^{13} K/s [83]. Samples were relaxed under NPT (constant pressure and temperature) ensemble. Nano-indentation was carried out on these samples with an indenter having a spherical tip (radius 20Å) up to a depth of 40Å along Y-direction. The MD simulation of nano-indentation was employed under NVT (constant volume and constant temperature) ensemble. The bottom part of sample was kept fixed to prevent the substrate from moving in the direction of indentation during the whole simulation. The size of substrate was 100 Å × 20 Å × 100 Å. Periodic boundary condition was applied in non-loading directions i.e., along X- axis and Z-axis. MD simulation of nano-indentation was carried out on MG and GMCs containing different volume fraction of crystallites as mentioned earlier to study its effect on mechanical properties of materials and deformation behaviour. The strain rates used for indentation were 2.5×10^{9} s^{-1}, 2.5×10^{10} s^{-1}, 1.25×10^{11} s^{-1} and 2.5×10^{11} s^{-1}. The simulation of nano-indentation comprised of indentation and equilibrium stages. In equilibrium stage the indenter was kept at a distance of 3 Å from sample in order to avoid long range attractive force between them. In the second stage the indenter moved downward to 43 Å at above mentioned strain rates. The motion of each atom was governed by Newton's second law of motion. Newton's law of motion was integrated by velocity-Verlet algorithm with a time-step of 0.002 ps. *P-h* curves were drawn for both types of samples at various strain rates to study the variation in mechanical properties like strength, yield point value, maximum load value and hardness. The EAM (embedded atom method) potential was used to describe the interaction between atoms. The total energy of an atom E_i is given by Mendelev et al. [74] as

$$E_i = F_\alpha \left(\sum_{j \neq i} \rho\beta(r_{ij}) \right) + \frac{1}{2} \sum_{j \neq i} \phi_{\alpha\beta}(r_{ij}) \text{ ----------------------------- } (3.10)$$

where, embedding energy F is a function of atom's electron density ρ . ϕ is a pair potential interaction, α and β are the element types of atoms *i* and *j*. It is a widely used potential for studying the properties of materials [19, 50]. All the simulations are carried out on LAMMPS platform which is a widely used open source code [80].

3.9. Work plan

The following Tables (Table 3.1, 3.2, 3.3) list various alloys and several nano-indentation parameters that are used to carry out the investigation.

Table 3.1. Parameters used in alloy model preparation for nano-indentation studies

Alloy	Cooling rate	Crystalline volume fraction (%)	Shape of crystallite and distribution	Size of the crystallite
Metallic glass				
$Zr_{50}Cu_{50}$	10^{13} K/s	-	-	-
$Zr_{50}Cu_{30}Al_{20}$	10^{13} K/s	-	-	-
Metallic glass matrix composites				
$Zr_{50}Cu_{50}$	10^{13} K/s	14	Spherical and randomly distributed	15 Å radius
$Zr_{50}Cu_{50}$	10^{13} K/s	30	Spherical and randomly distributed	21 Å radius
$Zr_{50}Cu_{50}$	10^{13} K/s	50	Spherical and randomly distributed	20 Å radius
$Zr_{50}Cu_{50}$	10^{13} K/s	14	Single spherical crystallite	32 Å radius

Alloy	Cooling rate	Crystalline volume fraction (%)	Shape of crystallite and distribution	Size of the crystallite
$Zr_{50}Cu_{50}$	10^{13} K/s	14	Cylindrical crystallites	10 Å radius and 100 Å length
$Zr_{50}Cu_{30}Al_{20}$	10^{13} K/s	14	Spherical and randomly distributed	15 Å radius
$Zr_{50}Cu_{30}Al_{20}$	10^{13} K/s	30	Spherical and randomly distributed	20 Å radius
$Zr_{50}Cu_{30}Al_{20}$	10^{13} K/s	50	Spherical and randomly distributed	20 Å radius

Table 3.2. Several parameters used for nano-indentation studies of metallic glass and glass matrix composites.

Alloy	Crystallite Volume fraction (%)	Temperature of deformation (K)	Strain rate (s^{-1})	Indenter diameter (Å)	Depth of Indentation (Å)
$Zr_{50}Cu_{50}$	0	100, 300, 500	2.5×10^{9} , 2.5×10^{10}, 1.25×10^{11}, 2.5×10^{11}	40	40
$Zr_{50}Cu_{50}$	14,30, 50	100, 300, 500	2.5×10^{9} , 2.5×10^{10}, 1.25×10^{11}, 2.5×10^{11}	40	40
$Zr_{50}Cu_{30}Al_{20}$	0	300	2.5×10^{9} , 2.5×10^{10}, 1.25×10^{11}, 2.5×10^{11}	40	40
$Zr_{50}Cu_{30}Al_{20}$	14,30, 50	300	2.5×10^{9} , 2.5×10^{10}, 1.25×10^{11}, 2.5×10^{11}	40	40

Table 3.3. Nomenclature used in the present study

Alloy	Volume fraction of crystallite	Nomenclature
$Zr_{50}Cu_{50}$	14	Composite-I
$Zr_{50}Cu_{50}$	30	Composite-II
$Zr_{50}Cu_{50}$	50	Composite-III
$Zr_{50}Cu_{30}Al_{20}$	14	Composite-IV
$Zr_{50}Cu_{30}Al_{20}$	30	Composite-V
$Zr_{50}Cu_{30}Al_{20}$	50	Composite-VI

CHAPTER 4

RESULTS AND DISCUSSIONS

MD simulations of nano-indentation on $Zr_{50}Cu_{50}$, $Zr_{50}Cu_{30}Al_{20}$ metallic glasses (MGs) and $Zr_{50}Cu_{50}$, $Zr_{50}Cu_{30}Al_{20}$ glass matrix composites (GMCs) with 14%, 30% and 50% crystalline volume fraction have been studied. Nano-indentation tests are conducted at varying strain rates (2.5×10^9 s^{-1}, 2.5×10^{10} s^{-1}, 1.25×10^{11} s^{-1} and 2.5×10^{11} s^{-1}) and temperatures (100K, 300K and 500K) to investigate the deformation behaviour and response on the mechanical properties such as yield point, maximum load, and hardness through load-displacement plots. Also, the effect of crystallite distribution (single-spherical and multi-spherical) and shape (spherical and cylindrical) on the load-displacement response have been studied. Structural analysis during deformation has been done by centro-symmetry parameter (CSP) studies. The validation of the Zr-Cu and Zr-Cu-Al potentials are performed before the study of alloy models. The procedure is described in the following paragraphs.

4.1. Validation of inter-atomic potentials

4.1.1. Validation of Zr-Cu inter-atomic potential

An MD simulation of $Zr_{50}Cu_{50}$ melting is performed to validate the Cu-Zr EAM-fs (Embedded Atom Method-Finnis Sinclair) potential that is used in the present study. The experimentally observed melting point of ~ 1226 K for $Zr_{50}Cu_{50}$ alloy is taken as the reference [65] and is input into the MD melting simulation code. The quantitative analysis of the structural changes during melting is monitored by RDF (radial distribution function) analysis at every 100 time-steps. RDF is a plot of atomic density g(r) with respect to inter-atomic separation (r). Figs. 4.1a and 4.1b shows the RDF plots of the structural changes taking place during melting. Fig. 4.1a shows the initial $Zr_{50}Cu_{50}$ structure. It can be seen that there are many sharp peaks, with the first peak having g(r) value of 18.4 approximately. This indicates crystalline structure [83]. At 1200 K (Fig. 4.1b) the intensity of the first peak is lower having peak with g(r) value of 2.6. Also, the first peak appears broader and rest others are diffused. This reveals the existence of liquid state [83] at 1200 K. Kao et al.[84] also found the melting point of $Zr_{50}Cu_{50}$ system to be 1211 K in the simulation of melting. So, in all the present MD simulations, a melting point of 2300 K, much above the observed has been taken for obtaining glassy structures by rapid cooling. Similarly, a temperature of 2000 K was used in Cu-Zr model melt-quench simulations[84].

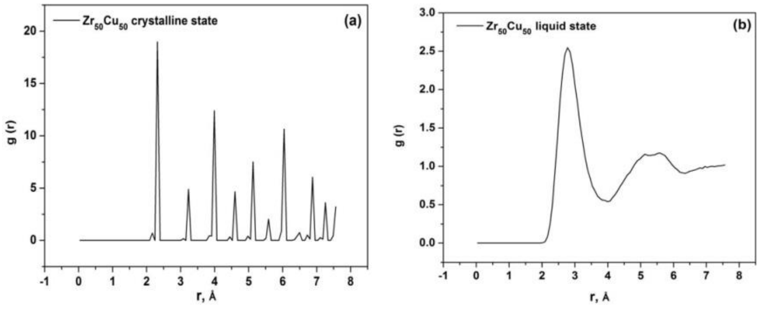

Figure 4.1. RDF plot of $Zr_{50}Cu_{50}$ metallic glass with (a) crystalline (b) liquid states

4.1.2. Validation of Zr-Cu-Al inter-atomic potential

An MD simulation of $Zr_{50}Cu_{30}Al_{20}$ melting is performed to validate the Cu-Zr-Al EAM-alloy (Embedded Atom Method-alloy) potential that is used in the present study. The experimentally observed melting point of $Zr_{53.9}Cu_{33.1}Al_{13}$ metallic glass is 1136 K [85]. So a temperature of 1200 K is taken as input into the MD melting simulation code. The structural changes during melting are monitored by RDF (radial distribution function) analysis at every 100 time-steps. A plot between g (r), and inter-atomic separation (r) is drawn as shown in Fig. 4.2 for the initial and the structure at 1200 K. It can be seen that RDF plot of the initial structure has several sharp peaks while structure at 1200 K has broad and diffused peaks. Therefore, it can be stated that the melting point of the alloy is ~1200 K which is comparable with that of the experimentally observed melting point. So, in the present study, the MD simulation for obtaining glassy structure in Zr-Cu-Al alloy is taken more than the observed i.e. 2300 K.

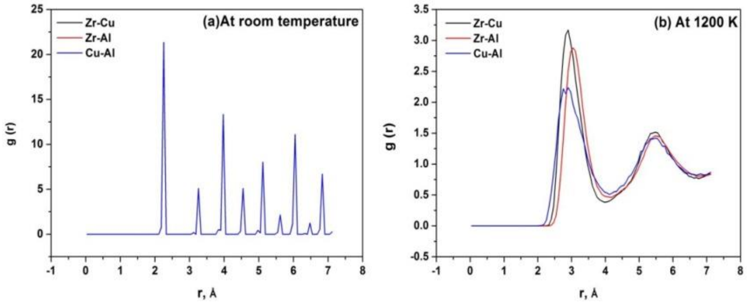

Figure 4.2. RDF plots of $Zr_{50}Cu_{30}Al_{20}$ metallic glass with (a) crystalline (b) liquid state.

4.2. Nano-indentation simulation studies of $Zr_{50}Cu_{50}$ metallic glass

The $Zr_{50}Cu_{50}$ crystalline alloy model was melted and quenched to obtain metallic glass (MG). It was then indented with a diamond indenter having a spherical tip (radius = 20Å) up to a depth of 40Å along Y-direction. The indentation was done at different strain rates i.e., 2.5×10^{9} s^{-1}, 2.5×10^{10} s^{-1}, 1.25×10^{11} s^{-1} and 2.5×10^{11} s^{-1} and at different temperatures in the range of 100 K-500 K to understand the load-displacement behaviour. Fig. 4.3 shows the atomic snapshot of the MG at initial (Fig. 4.3a) and after indentation at 2 ps (Fig. 4.3b).

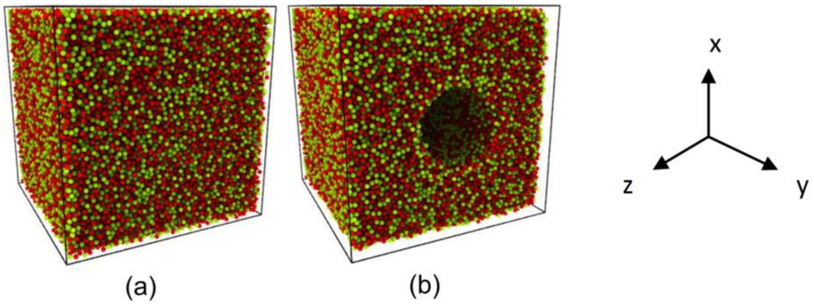

Figure 4.3. Atomic snapshots of $Zr_{50}Cu_{50}$ metallic glass (a) initial, (b) 2 ps.

4.2.1. Effect of strain rate on the load-displacement behaviour

Fig. 4.4 shows the load-displacement (*P-h*) plot of $Zr_{50}Cu_{50}$ metallic glass at varying strain rates and at 300 K. It shows a linear elastic behaviour and non-linear plastic behaviour at all the strain rates. As the depth of indentation increases, load on the indenter also increases. This shows that it obeys the Hertz's theory of elastic contact between two bodies within the elastic deformation region.

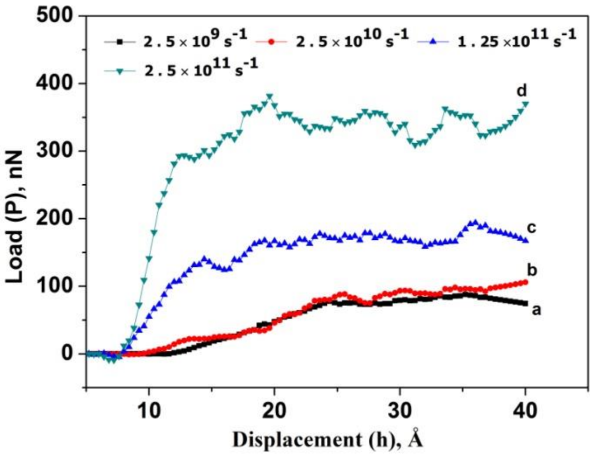

Figure. 4.4. *P-h* plot for $Zr_{50}Cu_{50}$ metallic glass at varying strain rates: (a) $2.5\times10^{9}s^{-1}$, (b**)** $2.5\times10^{10}s^{-1}$, (c)$1.25\times10^{11}s^{-1}$ and (d) $2.5\times10^{11}s^{-1}$.

The expression for the load is given by the following equation [50].

$$F = \frac{4}{3} r^{1/2} E^{*} h^{3/2} \text{ --- } (4.1)$$

where, '*F'* is load, '*r'* is the radius of indenter, '*E*'* is the reduced Young's modulus and '*h'* is the indentation depth. The non-linearity can be observed after the first "pop in" [86] event after which serrations or load drops appear, but in irregular fashion. This irregularity may be due to lack of long range order of atomic arrangement in metallic glass. The point of first load drop is called the yield point [87] . The phenomenon of serration is caused by inhomogeneous plastic deformation. The serration in *P-h* curves of $Zr_{50}Cu_{50}$ metallic glass at varying strain rate is coherent with the simulation result presented by Jiang et al. [16]. Serrations are present in all the curves at different strain rates but with increase of strain rate to 1.25×10^{11} s^{-1} and 2.5×10^{11} s^{-1} (Fig. 4.4c and 4.4d), they appear to be oscillating about certain fixed value of load viz. 150 nN and 350 nN respectively. It does not show an increase in load bearing capacity i.e., load value is constant with increase of depth of indentation. This is due to strain softening with load fluctuating about a constant value. The same trend that after a certain indentation depth, load carried by the sample fluctuate about a certain value was observed in the studies of Qiu et al [50]. Further, the maximum load value increases with increase in strain rate. With increase of strain rate the atoms are displaced far away at every time-step. Atoms do not get enough time to recover or adjust. The ability of sample to resist deformation appears stronger. The rise of strain rate thus leads to hardening of sample and thus an increase in maximum load values. The same behaviour can be observed in simulation studies of Qiu et al. [50].

Table 4.1. Comparison of load at different depth of nano-indentation of Zr-Cu and Zr-Cu-Al MGs with literature.

References	Jiang et al., 2008 [16]	Qiu et al., 2014 [50]	Wu et. al, 2015 [88]	Present study		
Alloy system	$Cu_{46}Zr_{54}$	$Cu_{50}Zr_{50}$	$(CuZr)_{95}Al_5$	Zr_{50} Cu_{50}		
Potential	LJ	LJ	LJ	EAM		
Box size (Å^3)/atoms	250×250× 125/432,000	210×150 ×120	300 × 300 × 80	100×100×100/90,000		
Indenter type/ radius (Å)	Spherical/20	Spherical/30	conical	Spherical/20		
Strain rate, s^{-1}	1×10^{11}	2.5×10^{10}	1.25×10^9	1.25×10^{11}	2.5×10^{10}	2.5×10^9
Indentation depth (Å)	14	25	40	14	25	40
Load (nN)	70	180	440	130	86	371
Temperature , K	300	293	300	300		
Boundary condition	Periodic in X and Z direction	Periodic in X and Y direction	Periodic in X and Y direction	Periodic in X and Z direction		

Table 4.1 shows the comparative study on the load values at a particular depth of indentation of metallic glasses and crystalline material in the literature with the present study at various parameters such as strain rate, temperature and indenter diameter. It can be seen that the observed values at the same strain rate are different to that reported in the literature. This could be due to the difference in sample dimensions, potential used and indenter diameter.

4.2.2 Effect of temperature on load-displacement response

The *P-h* plot of $Zr_{50}Cu_{50}$ metallic glass sample indented at varying temperatures of 100K, 300K and 500K and at a constant indentation strain rate of 2.5×10^{10} s^{-1} is shown in Fig.4.5.

The metallic glass indented at 100K has a higher yield point than that of the other two at 300K and 500K which shows that yield point decreases with increase in temperature. This behaviour is due to the fact that atoms move far away as the temperature is increased so that interaction between them weakens which leads to increase in plasticity or alloy become softer [50].

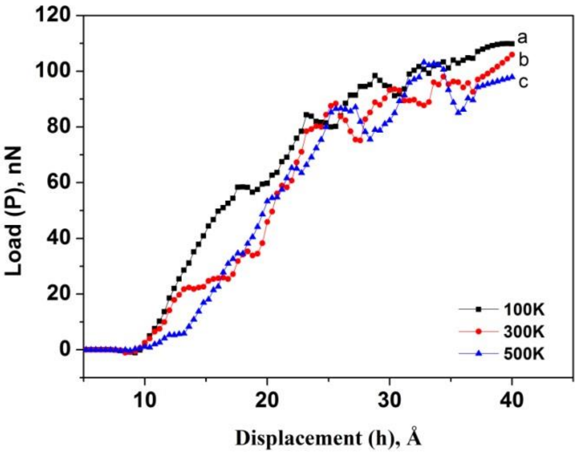

Figure 4.5. *P-h* plot of $Zr_{50}Cu_{50}$ based metallic glass nano-indented at strain rate of 2.5×10^{10} s^{-1} and temperatures of (a) 100 K, (b) 300 K and (c) 500 K.

It can be observed that the amplitude of flow serrations increase as the temperature is increased. This could be attributed to the fact that atomic vibration increase with temperature rise and cause more fluctuation in loads. Also, these load drops are not at regular intervals because of glasses having short range order arrangement of atoms [89].

4.3. Nano-indentation simulation studies of Zr-Cu metallic glass matrix composites

Nano-indentation simulation studies of Zr-Cu metallic glass matrix composites with different crystalline volume fractions (14%, 30% and 50%) were carried out at different strain rates

($2.5\times10^{9}s^{-1}$, $2.5\times10^{10}s^{-1}$, $1.25\times10^{11}s^{-1}$, and $2.5\times10^{11}s^{-1}$) and temperatures (100 K, 300 K and 500 K) in order to understand the influence of crystallites on the load-displacement behaviour. Further, centro-symmetry parameter studies were carried out to analyze the structural changes taking place in the crystallite during nano-indentation.

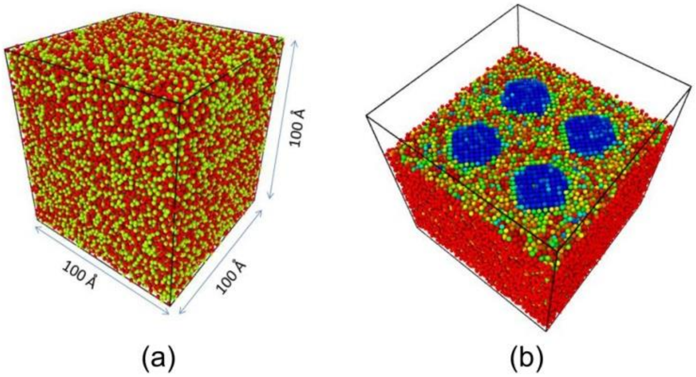

Figure 4.6. (a) Atomic position snap shots of the $Zr_{50}Cu_{50}$ MGMC with complete simulation box (red coloured atoms: Zr; green coloured atoms: Cu) ; (b) sliced box revealing the crystallites position (the atoms are coloured based on the centro-symmetry parameter values (blue colour: no defect; red coloured: defect)

Fig.4.6a shows the atomic position snapshot of $Zr_{50}Cu_{50}$ based GMC with 14% crystallite volume fraction. Fig. 4.6b shows the sliced view of the composite with spherical crystallites (blue coloured) embedded in the amorphous matrix. The crystallite is a group of ordered atoms having FCC crystal structure. Hereafter, this composite is termed as composite-I. Similarly, GMCs with 30% are termed as composite-II and 50% as composite-III. Nano-Indentation is carried out along Y-direction with periodic boundary conditions in non-loading direction.

4.3.1. Effect of strain rate on load-displacement response

4.3.1.1. Composite-I (14% crystallites)

Composite-I was loaded under varying strain rates, and the *P-h* plot (Fig. 4.7) was drawn to observe the deformation behaviour. It can be seen that all the curves shows linear elastic behaviour and non-linear plastic behaviour. In the elastic region the curve obeys Hertzian contact theory and thus load value rises linearly with indentation depth [50]. The non-linearity in curve is observed after the first "pop in" or load drop which indicates the onset of plastic yielding occurring in alloy [86]. "Pop in" or load drops are present in all the curves but at the strain rate of 1.25×10^{11} s^{-1} (Fig.4.7c) they appear to be oscillating about a load of 140 nN after a depth of 24 Å. As the strain rate is increased further to 2.5×10^{11} s^{-1} (Fig.4.7d), there is decrease in load after maximum load (20 Å). This may be due to strain softening. Amorphous phase which is high in volume fraction, bears the load first besides transferring to crystallites, softens when plastic deformation occurs after yield point. Load transferred to

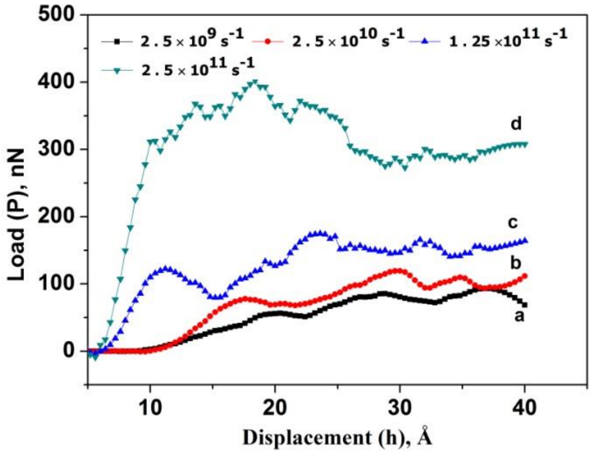

Figure 4.7. *P-h* plot for composite-I at varying strain rates: (a) $2.5\times10^{9}s^{-1}$, (b) $2.5\times10^{10}s^{-1}$, (c) $1.25\times10^{11}s^{-1}$ and (d) $2.5\times10^{11}s^{-1}$.

crystallites simultaneously cause obstruction to deformation initially until deformed plastically to amorphous state [25] up till the maximum load value. This lead to strain hardening after the yield point. Thereafter, drop in the load occurs indicating strain softening after maximum load.

4.3.1.2. Composite-II (30% crystallites)

Fig. 4.8 shows the *P-h* curve of composite-II indented at different strain rates and at 300 K. It can be seen that the curves show linear elastic behaviour and non-linear plastic behaviour up to a displacement of 40 Å. The curve shows gradual rise in the load with depth of indentation following Hertzian contact theory in elastic region [50]. At lower strain rates (Fig 4.8a and 4.8b), there is increase in load value continuously with indentation depth but not much pronounced. The yield point value as well as maximum load values show a rise as the strain rate is increased. The Amorphous phase bears load first along with transferring to crystallites. Crystallites coming in the path cause obstruction to deformation till it deforms plastically [25]. As crystallites and matrix phase are deformed completely at the maximum load, strain softening occurs (Fig 4.8c and 4.8d). It can be seen that amplitude of serrations decrease with increase in strain rate. This may be due to atoms not getting enough time to rearrange. Also, the serrations in the curve are not at regular intervals at all strain rates. This may be attributed to the fact that glassy structure has short range order [89]. Yield point value is higher at different strain rates than that of composite-I due to higher volume fraction of crystallites obstructing the movement of atoms in the glass matrix.

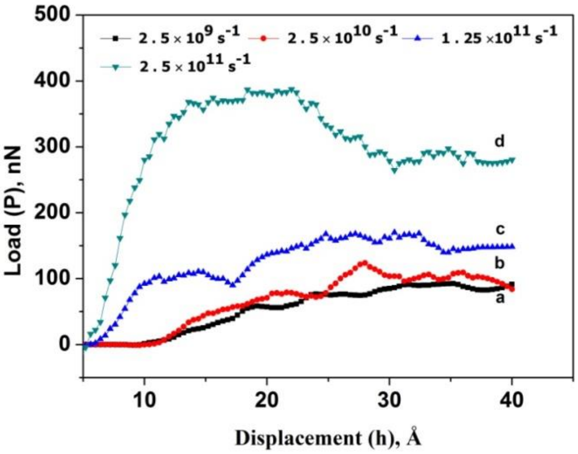

Figure 4.8. *P-h* plot for composite-II at varying strain rates: (a) $2.5\times10^{9}s^{-1}$, (b) $2.5 \times10^{10}s^{-1}$, (c) $1.25\times10^{11}s^{-1}$ and (d) $2.5\times10^{11}s^{-1}$.

4.3.1.3. Composite-III (50% crystallites)

Figure 4.9 shows the load-displacement plot of composite-III indented at different strain rates during loading. The *P-h* curves show a linear elastic behaviour and non-linear plastic behaviour. There is increase in load on indenter with the displacement value in elastic region which obeys Hertzian contact theory [50]. As the strain rate is increased (Fig. 4.9c and 4.9d); the rise in load become more pronounced as compared to at lower strain rates (Fig. 4.9a and 4.9b). This may be due to delay in load transfer from matrix to crystallites. The curve shows a fluctuating nature about some fixed load in the displacement range of 10Å-30Å. This may be so because the amorphous phase which is equal in volume fraction to crystallites bears the load first and transfer it to crystallites in a short span. But, these crystallites also get deformed to a much extent along with matrix phase till the yield point is reached. It also leads to lesser strain hardening (Fig. 4.9d) as compared to composite-I and composite-II. This can be observed with a lesser maximum load at the same strain rate. Curve appears flat just after the yield point, and finally strain softening is observed after 30 Å of displacement.

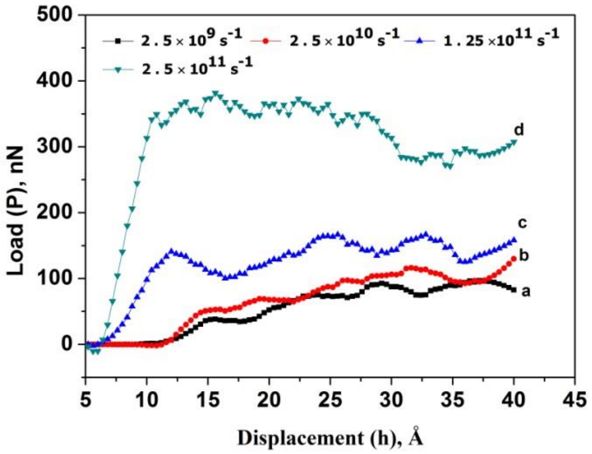

Figure 4.9. *P-h* plot for composite-III at varying strain rates: (a) $2.5\times10^{9}s^{-1}$, (b) $2.5\times10^{10}s^{-1}$, (c) $1.25\times10^{11}s^{-1}$ and (d) $2.5\times10^{11}s^{-1}$.

4.3.1.4. CSP (centro-symmetry parameter) analysis of composite-I

Figure 4.10 shows the atomic snapshots of $Zr_{50}Cu_{50}$ based composite-I at different depth of indentation at various strain rates, i.e., 2.5×10^{9} s^{-1}, 2.5×10^{10} s^{-1}, 1.25×10^{11} s^{-1} and 2.5×10^{11} s^{-1}. The centro-symmetry parameter (CSP) is used for analysis of the structural changes during indentation. The colour coding is done according to the intensity of defects. CSP value of zero indicates no defects while CSP value of twelve indicates surface and stacking fault defects [81]. The red and green atoms surrounding the blue circular region (crystallite) is $Zr_{50}Cu_{50}$ metallic glass matrix. The crystallite initially is free of defects (Fig. 4.10a (i), 4.10b (i), 4.10c (i) and 4.10d (i)); but with progress of indentation plastic deformation of the crystallites occur at all strain rates along with that of glassy matrix. Crystallites deform plastically by the initiation and movement of defects such as dislocations as witnessed by the change in the colour of the atoms from blue to red. Finally, the crystallites are seen

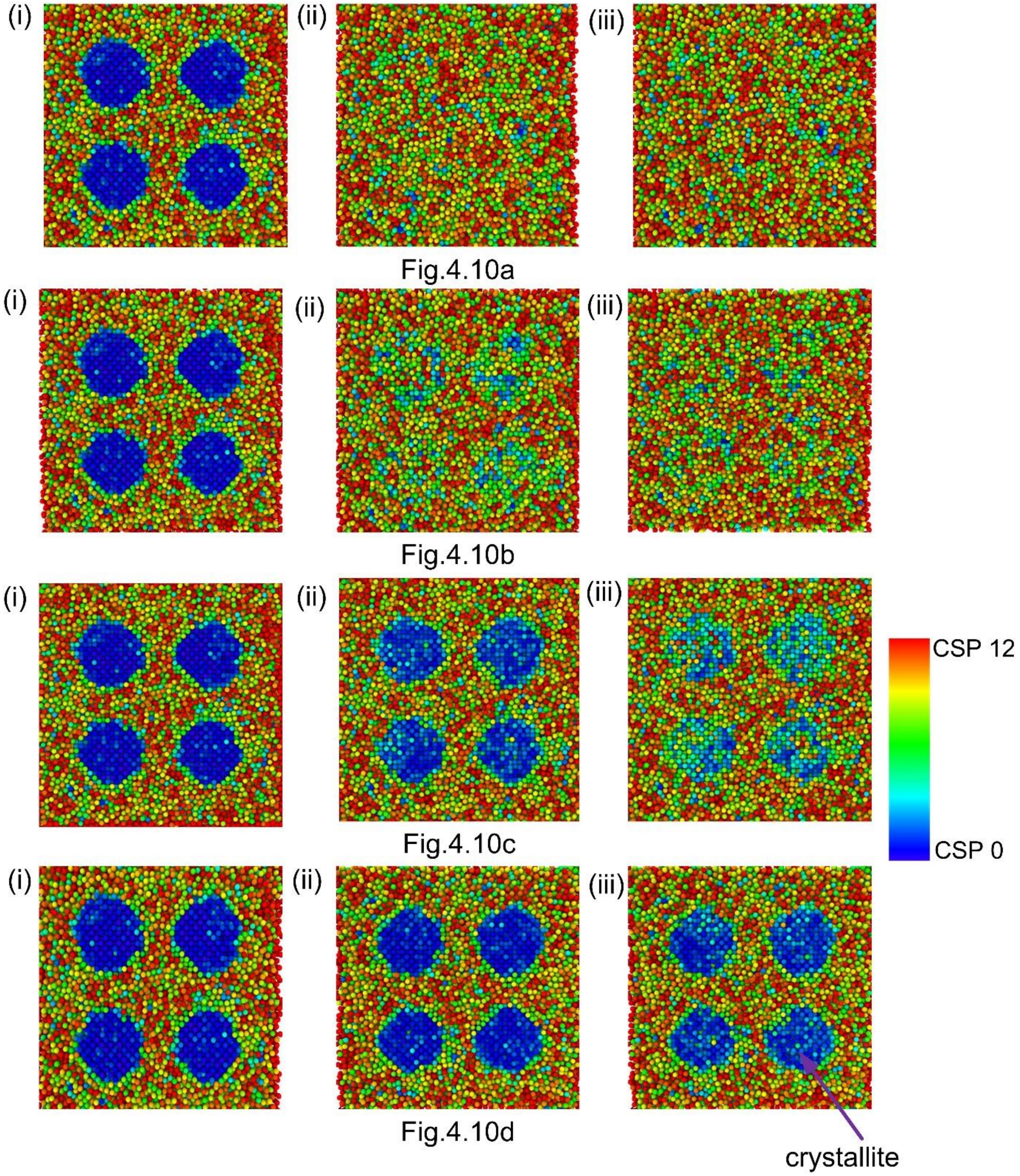

Fig.4.10a

Fig.4.10b

Fig.4.10c

Fig.4.10d

Figure 4.10. Atomic snapshots of the $Zr_{50}Cu_{50}$ metallic glass matrix composites containing 14 % crystallites at different depth of indentation (i) initial, (ii) 0.4 Å, (iii) 0.8 Å; and at different strain rates: 2. 5×10^9 s^{-1} (Fig. 4.10a), 2.5×10^{10} s^{-1} (Fig. 4.10b), 1.25×10^{11} s^{-1} (Fig. 4.10c) and 2. 5×10^{11} s^{-1} (Fig. 4.10d)

becoming amorphous (Fig. 4.10a (iii), 4.10b (iii), 4.10c (iii)) with progress of deformation. Further, the defect density decreases with increasing strain rate (Fig. 4.10c (iii) and 4.10d (iii)). In Fig. 4.10d (iii), the crystallites appear to have less number of defects as compared to the case with lower strain rates at the same indentation depth of 0.8 Å. So, it can be stated that at higher strain rates, load transfer from matrix to crystallites is delayed as compared to that at low strain rates.

4.3.2. Effect of temperature on load-displacement response

4.3.2.1 Composite-I (14 % crystallites)

Composite-I is indented at temperatures of 100 K, 300 K and 500 K and at strain rate of 2.5×10^{10} s^{-1}. The corresponding *P-h* curves are shown in Fig. 4.11. The curves show linear elastic behaviour and non-linear plastic behaviour and follow the Hertzian contact theory [50] in the elastic region of indentation. It is observed that, as the temperature is increased

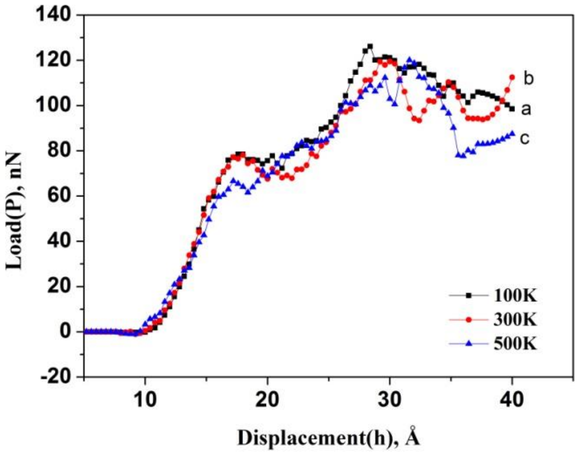

Figure 4.11. *P-h* plot of composite-I nano-indented at strain rate of 2.5×10^{10} s^{-1} and at temperature values of (a) 100K, (b) 300 K and (c) 500 K..

from 100 K to 500 K, curves show a decrease in maximum load value at different displacements of indenter. This indicates softening of the composite with increase of temperature and so the load bearing capacity decreases. The yield point also decreases with increasing temperature. This indicates that the compressive strength of composite-I is decreasing with temperature rise. Further, the amplitude of serrations increase with temperature rise [90]. This is attributed to the atomic vibrations at higher temperature. Moreover, strain hardening in the composite can be observed in all the curves with increase of depth of indentation

4.3.2.2. Composite-II (30 % crystallites)

Fig. 4.12 shows the *P-h* plot of composite-II at temperatures of 100 K, 300 K and 500 K. Curves show an increase in load on indenter with depth of indentation. All curves follow Hertzian contact theory in the elastic region and so load is increasing with displacement [50].

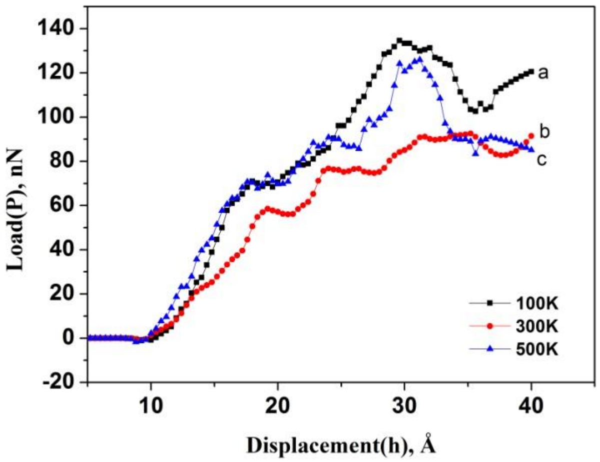

Figure 4.12. *P-h* plot of composite-II nano-indented at strain rate of $2.5\times10^{10}\ s^{-1}$ and at temperature values of (a) 100K, (b) 300 K and (c) 500 K.

Further, at temperature of 300 K the initial slope of the *P-h* curve is lower compared to the others. This could be due to structural changes. Also, strain hardening is observed after indentation depth of 20 Å at all temperatures.

4.3.2.3. Composite-III (50 % crystallites)

The load-displacement plot of composite-III indented at varying temperatures of 100 K, 300 K and 500 K is shown in Fig. 4.13. The curves show linear elastic behaviour and non-linear plastic behaviour. There is increase in load on indenter with increasing depth of indentation in the elastic region. This is because the curve follows Hertzian contact theory [50]. The amplitude of serrations in *P-h* curve increases with increase of temperature to 500 K (Fig. 4.13) [90]. Here, the slope of initial portion of curves appears same at different temperatures. There is no significant effect of temperature on the yield point and maximum load.

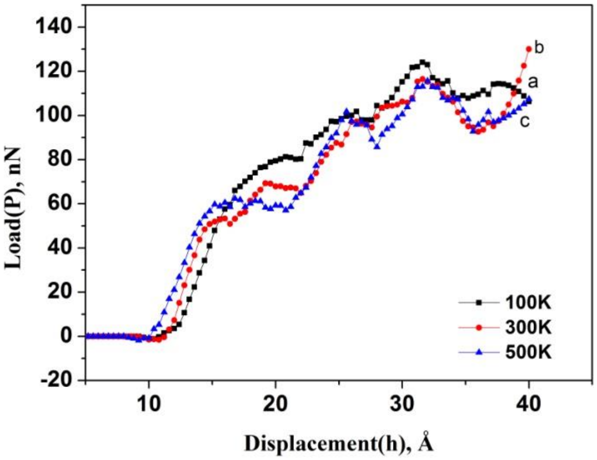

Figure 4.13. *P-h* plot of composite-III nano-indented at strain rate of 2.5×10^{10} s^{-1} and at temperature values of (a) 100K, (b) 300 K and (c) 500 K.

4.3.3 Effect of crystallite distribution and shape

4.3.3.1. Effect of presence of a single crystallite in $Zr_{50}Cu_{50}$ based GMC

Fig.4.14. shows the atomic position snap shots of $Zr_{50}Cu_{50}$ metallic glass composite in full (Fig.4.14a) and sliced view (Fig. 4.14b). Spherical crystallite (blue coloured) of 32 Å radius is embedded at the centre occupying 14 % volume fraction. Fig.4.15 shows the curves of load applied on the indenter (*P*) Vs depth of indentation (*h*) in the $Zr_{50}Cu_{50}$ metallic glass composite sample indented at strain rates of 2.5×10^{10} s^{-1}, 6.25×10^{10} s^{-1} and 1.25×10^{11} s^{-1}. All the curves show linear elastic behaviour and non-linear plastic behaviour. Elastic behaviour is shown up to first load drop in the curves. The load on indenter increases with indentation depth according to Hertz's contact theory before the beginning of plastic deformation [50]. The curve changes its slope after the first load drop indicating plastic deformation occurring with further loading. The load drops are irregularly spaced in all curves which may be due to short range order structure of GMCs. The maximum load value

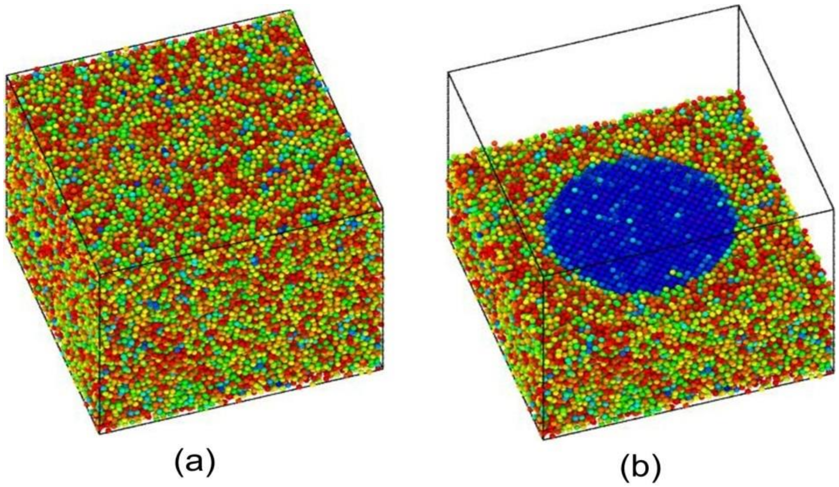

Figure 4.14. Atomic position snap shots of the $Zr_{50}Cu_{50}$ metallic glass composite: (a) complete simulation box (red coloured atoms: Zr; green coloured atoms: Cu; (b) sliced box revealing the central crystallite position (the atoms are coloured based on the centro-symmetry parameter values (blue colour: perfect crystal)).

increases with increase in strain rate of indentation. This could be due to delay in load transfer from matrix to crystallites with the rise in strain rate. Crystallites bear further load after yield point until amorphized reaching maximum load.

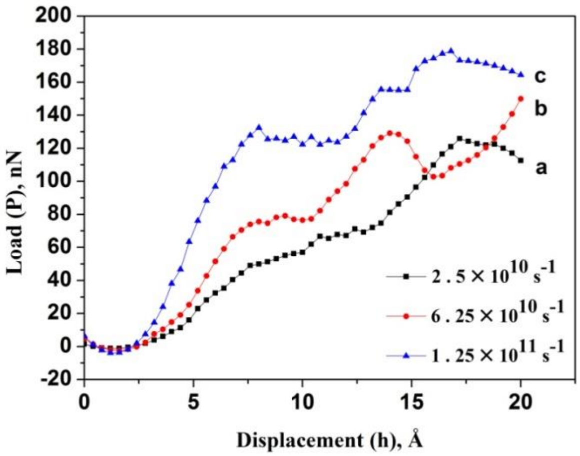

Figure 4.15. *P-h* plot of $Zr_{50}Cu_{50}$ metallic glass composite containing mono-crystallite (14%) at different strain rates: (a) 2.5 × 10^{10} s^{-1}; (b) 6.25 × 10^{10} s^{-1}; (c) 1.25 × 10^{11} s^{-1}.

To compare the effect of distribution of crystallites in form of a single crystallite and multi-spherical crystallites on mechanical properties, a *P-h* plot was drawn as shown in Fig. 4.16. It can be observed that there is a clear difference in the curves, as composite with single-spherical crystallite appears to bear a higher load at every point of displacement of indenter. It reveals that a composite with crystallite in form of mono-sphere has higher strength as compared to composite containing same volume fraction of crystallites in multi-spherical form. This could be due to the obstruction caused to movement of atoms in the glass matrix by single-crystallite is more than that in multi-spherical crystallites.

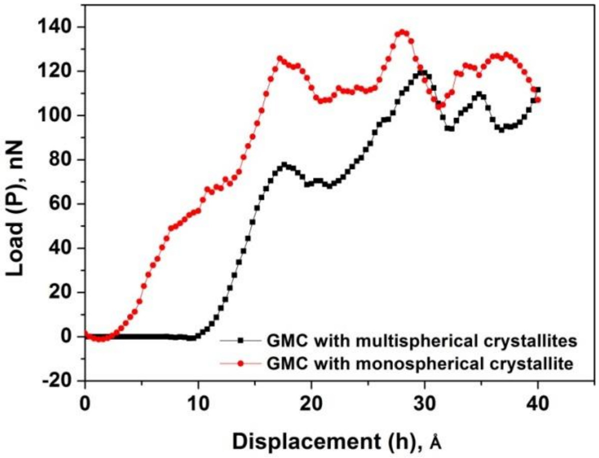

Figure 4.16. Comparison of *P-h* plot response of GMCs containing 14 % crystallite in form of mono-sphere and multi-sphere indented at 2.5× 10^{10} s^{-1}.

4.3.3.2. Effect of crystallite shape on the load-displacement plot of $Zr_{50}Cu_{50}$ based composite

Figure 4.17 shows the atomic snapshots of $Zr_{50}Cu_{50}$ based GMC containing crystallites in spherical and cylindrical forms when there are no defects or deformation in the sample. The colour index of blue shows no defect or crystallite in form of cylinders and sphere while other colour index like green, yellow red makes the matrix phase.

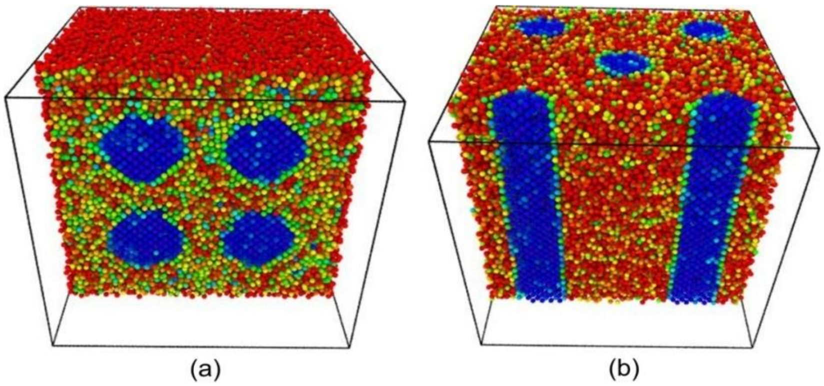

Figure 4.17. Atomic snapshots of $Zr_{50}Cu_{50}$ based GMC containing crystallites in (a) spherical and (b) cylindrical forms. CSP value of 0 indicates no defect (blue); CSP value of 12 indicates surface defect (red).

The effect of crystallite shape (here spherical and cylindrical) on the load-displacement plot (Fig. 4.18) and mechanical properties have been investigated. The two curves show a linear elastic behaviour and nonlinear plastic behaviour. Yield point as well as maximum load is higher in case of composites containing cylindrical crystallites (reinforcement) rather than spherical crystallites of same volume fraction (Table 4.2). The reason for the above could be due to fact that cylindrical shape crystallites act as continuous reinforcements [91].

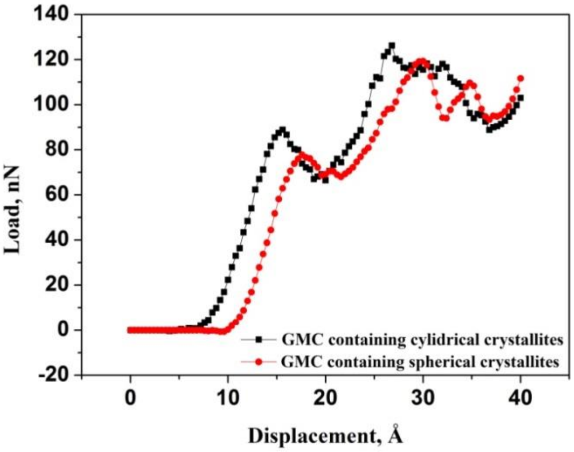

Figure 4.18. *P-h* plot showing GMC with 14 % by volume of spherical and cylindrical crystallites indented at $2.5\times10^{10}s^{-1}$ and at 300K.

Table 4.2. Yield point and maximum load value for $Zr_{50}Cu_{50}$ GMC containing crystallites in cylindrical and spherical forms indented at $2.5\times10^{10}s^{-1}$

	Yield point (nN)	Maximum load (nN)
GMC containing cylindrical crystallites	87.9	127.7
GMC containing spherical crystallites	74.5	120.4

4.4 Nano-indentation simulation studies of Zr-Cu-Al metallic glass

4.4.1 Effect of strain rate on load-displacement response

All the *P-h* plots show a linear elastic behaviour and non-linear plastic behaviour (Fig. 4.19). In the elastic region curves follows the Hertzian contact theory and so the load value increases with increase of displacement of indenter [50]. The plastic behaviour is shown from the first “pop in” event occurring in the curves as shown in Fig. 4.19. This point is called the yield point [87] whose value increases with increase in strain rate as shown from Fig. 4.19a to Fig. 4.19d. These serrations are irregularly spaced in each case due to short range order of metallic glass system [92]. There is strain softening (decrease in load) in material at high strain rate as seen from the curve (Fig. 4.19d). Maximum load value increases with increase of strain rate. This is so because the atoms are displaced farther away, so that they cannot return to their original position in short time and resistance to deformation increases [50].

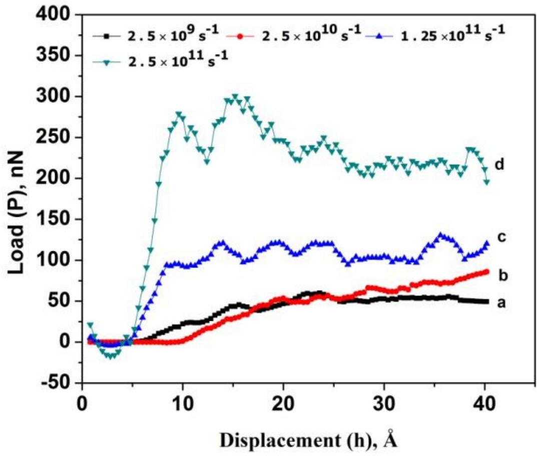

Figure 4.19. Load-displacement plot for $Zr_{50}Cu_{30}Al_{20}$ based metallic glass indented at varying strain rates from a to d; (a) $2.5\times10^{9}\ s^{-1}$, (b) $2.5\times10^{10}\ s^{-1}$, (c) $1.25\times10^{11}\ s^{-1}$, (d) $2.5\times10^{11}\ s^{-1}$.

4.5. Nano-indentation simulation studies of Zr-Cu-Al metallic glass matrix composites

4.5.1. Effect of strain rate on load-displacement response

4.5.1.1. Composites-IV (14 % crystallites)

The *P-h* curves exhibit a linear elastic behaviour and non-linear plastic behaviour as shown in Fig. 4.20. In the elastic region the curve follows the Hertzian contact theory, according to which load on indenter is proportional to the displacement of indenter in that direction [50].

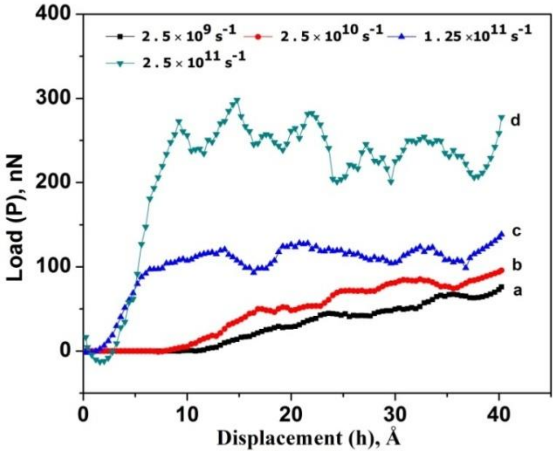

Figure 4.20. *P-h* plot for composite-IV indented at varying strain rates: (a) $2.5\times10^{9}\ s^{-1}$, (b) $2.5\times10^{10}\ s^{-1}$, (c) $1.25\times10^{11}\ s^{-1}$, (d) $2.5\times10^{11}\ s^{-1}$.

The first drop in the load is an indication of the onset of plastic deformation. Serration in all the curves are irregularly spaced due to short range order of glassy structure [92]. Curves show a gradual rise in load with displacement and this become more pronounced as the strain rate is increased (Fig. 4.20d). This may be so because with increase of strain rate load transfer from amorphous matrix to crystallites is delayed. Crystallites bear load along with matrix till the yield point. Further load is carried by crystallites which deform plastically until the maximum load is reached and become amorphous fully. There occur strain softening as all the crystallites are deformed after 15 Å of displacement. This can be observed by the decrease in load value after this distance of indentation.

4.5.1.2. Composite-V (30 % crystallites)

Composite-V indented at various strain rates and load-displacement plot was drawn as shown in Fig. 4.21. It shows linear behaviour in elastic region and obeys the Hertzian contact theory [50].

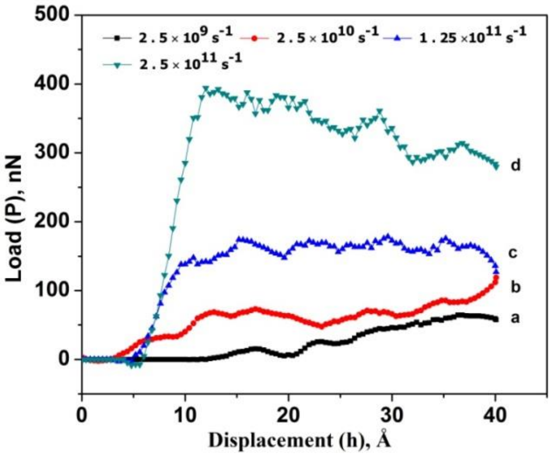

Figure 4.21. *P-h* plot for composite-V indented at varying strain rates: (a) 2.5×10^{9} s^{-1}, (b) 2.5×10^{10} s^{-1}, (c) 1.25×10^{11} s^{-1}, (d) 2.5×10^{11} s^{-1}.

The first load drop or "pop in" gives the onset of plastic deformation after which curves show nonlinear behaviour [86]. Load drop or serrations occur which are irregularly spaced. This may be due to lack of long range order in glassy alloys [92]. Though, the yield point rises as the strain rate is increased (Fig. 4.21c and 4.21d), the curves show a fall of load after reaching maximum load. This can be explained by the strain softening phenomena.

4.5.1.3. Composite-VI (50 % crystallites)

Figure 4.22 shows a *P-h* plot drawn to understand the deformation behaviour of composite-VI indented at varying strain rates. It shows a linear elastic behaviour and non-linear plastic behaviour. The onset of plastic yield occurs at the first “pop in” or load drop [86].

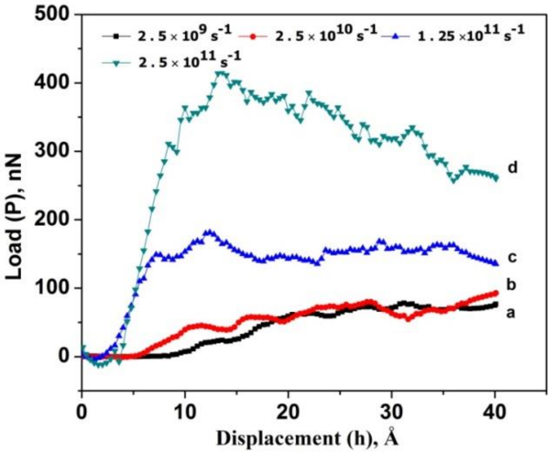

Figure 4.22. *P-h* plot for composite-VI indented at varying strain rates: (a) 2.5×10^{9} s^{-1}, (b) 2.5×10^{10} s^{-1}, (c) 1.25×10^{11} s^{-1}, (d) 2.5×10^{11} s^{-1}.

The curves follow Hertzian contact theory in elastic region as load is increasing with increase of depth of indentation [50]. As the strain rate is increased, amorphous phase of composite bears the load at first and then transfer it to crystallites in a short span as crystallites are comparably equal in volume fraction. The yield point is lower in case of composite-VI as compared to composite-V at 2.5×10^{11} s^{-1}. This shows that amorphous phase is deformed earlier and so the load is borne by the crystallites till the maximum load is reached and then strain softening occur as all the crystallites become amorphous due to deformation.

4.5.2. Effect of temperature on load-displacement response

4.5.2.1. $Zr_{50}Cu_{30}Al_{20}$ amorphous alloy

Fig. 4.23 shows the *P-h* plot of $Zr_{50}Cu_{30}Al_{20}$ amorphous alloy at temperatures of 100 K, 300 K and 500 K. Curves show an increase in load on indenter with depth of indentation. All curves follow Hertzian contact theory in the elastic region and so load is increasing with displacement [50]. The metallic glass indented at 100K has a higher yield point than that of the other two at 300K and 500K which shows that yield point decreases with increase in temperature.

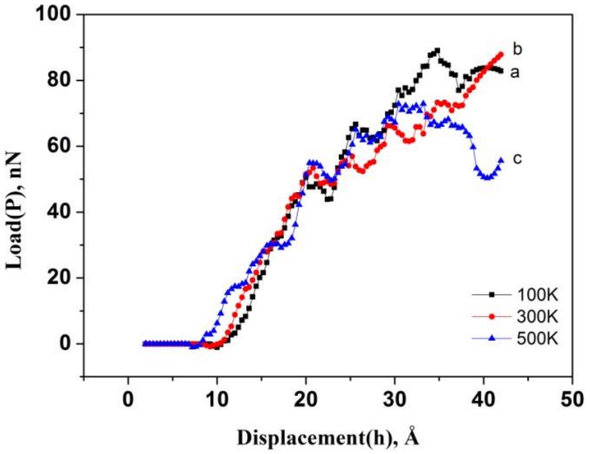

Figure 4.23. *P-h* plots of $Zr_{50}Cu_{30}Al_{20}$ amorphous alloy nano-indented at a strain rate of 2.5×10^{10} s^{-1} and at temperature values of (a) 100K, (b) 300 K and (c) 500 K.

4.5.2.2. Composite-IV (14% crystallites)

The *P-h* plot of composite-IV (14 % crystallites) sample indented at varying temperatures of 100K, 300K and 500K and at a constant indentation strain rate of 2.5×10^{10} s^{-1} is shown in Fig.4.24. At a temperature of 100 K the alloy shows a high yield point as compared with at 300 K and 500K. The first “pop in” occurring in plots give the yield point of alloy. These "pop in" or serrations are irregularly spaced due to the short range order arrangement of atoms.

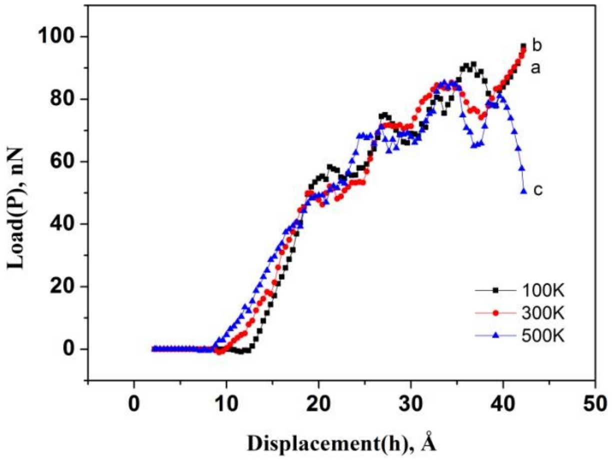

Figure 4.24. *P-h* plot of composite-IV nano-indented at strain rate of 2.5×10^{10} s^{-1} and at temperature values of (a) 100K, (b) 300 K and (c) 500 K.

4.5.2.3. Composite-V (30% crystallites)

Fig. 4.25 shows the *P-h* plot of $Zr_{50}Cu_{30}Al_{20}$ amorphous alloy at temperatures of 100 K, 300 K and 500 K. Curves show an increase in load on indenter with depth of indentation. All

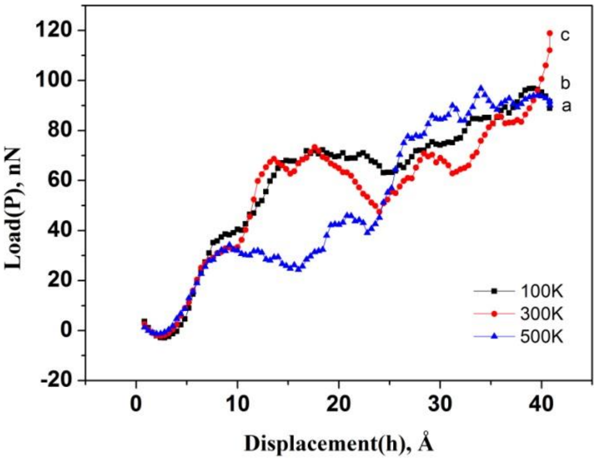

Figure 4.25. *P-h* plot of composite-V nano-indented at strain rate of 2.5×10^{10} s^{-1} and at temperature values of (a) 100K, (b) 300 K and (c) 500 K.

curves follow Hertzian contact theory in the elastic region and so load is increasing with displacement [50].

4.5.2.4. Composite-VI (50% crystallites)

Figure 4.26 shows the *P-h* plot of composite-VI nano-indented at strain rate of 2.5×10^{10} s^{-1} and at temperature values of 100K, 300K and 500K. Different curves show a linear elastic behaviour and non-linear plastic behaviour. There is rise in load value with displacement of indenter following Hertz's contact theory in all curves [50]. The curve at 100K has a high value of load at all point of displacement as compared with 300K and 500K. As the temperature rises curve shows a fall in yield point. "Pop in" are observed in different curves after yield point.

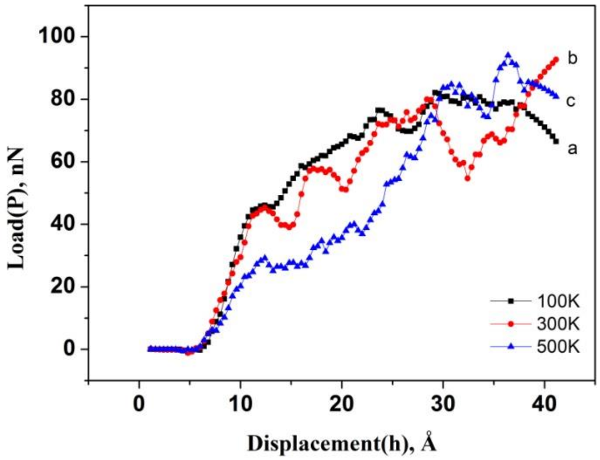

Figure 4.26. *P-h* plot of composite-VI nano-indented at strain rate of 2.5×10^{10} s^{-1} and at temperature values of (a) 100K, (b) 300 K and (c) 500 K.

4.6. Mechanical properties of Zr-Cu based MG and GMCs

4.6.1. Effect of strain rate on the yield point and maximum load

Mechanical properties such as yield point, maximum load, hardness of metallic glass and composite samples based on the above explained graphs are presented in a Tabular form for comparison and interpreting the mechanical behaviour. From Table 4.6, it can be seen that all samples either MG or GMCs show a rise in yield point value with strain rate. At strain rates of $2.5\times10^{9}s^{-1}$, $2.5\times10^{10}s^{-1}$ and $1.25\times10^{11}s^{-1}$ yield point value for metallic glass is higher than those of composites. Composite-III shows the lowest yield point value amongst all other composite samples at 2.5×10^{9} s^{-1} and 2.5×10^{10} s^{-1} strain rates. But a sudden rise of yield point is observed at strain rate of $1.25\times10^{11}s^{-1}$. At strain rate of $2.5\times10^{11}s^{-1}$ all the composites show higher yield point value as compared to the metallic glass and composite-III exhibits the highest yield strength. This anomalous behaviour of composite-III may be due to the delayed load transfer. More is the crystallite volume fraction, at high strain rate; more is available time to amorphize all the crystallites and higher will be the yield point.

Table 4.3 Yield point value of $Zr_{50}Cu_{50}$ based metallic glass and composites at various strain rates

Strain rate (s^{-1})	Yield point (nN)			
	Metallic glass	Composite-I	Composite-II	Composite-III
2.5×10^{9}	77.3	54.2	58.0	38.4
2.5×10^{10}	87.9	76.6	78.7	49.4
1.25×10^{11}	139.4	123.3	103.8	140
2.5×10^{11}	292.4	310.6	317.6	351.5

Table 4.4 shows the maximum load values of MG and GMCs. It can be seen that maximum load values increase with increase in strain rates. At strain rates of 2.5×10^{9} s^{-1} and 2.5×10^{10} s^{-1} composites have higher maximum load value as compared to MG. But as the strain rate is increased to $1.25\times10^{11}s^{-1}$ metallic glass has higher maximum load value than any of the composites. Also, composites are showing a decrease in maximum load value with increase

in crystallite volume fraction at strain rates of $1.25\times10^{11}s^{-1}$ and $2.5\times10^{11}s^{-1}$. This could be due to amorphization of the crystallites till the yield point is reached.

Table 4.4 Maximum load value of $Zr_{50}Cu_{50}$ metallic glass and composites at various strain rates

Strain rate (s^{-1})	Maximum load values (nN)			
	Metallic glass	Composite-I	Composite-II	Composite-III
2.5×10^{9}	88.3	94.5	94.5	97.8
2.5×10^{10}	106.8	120.9	125.9	131.2
1.25×10^{11}	196.1	176.2	170.4	167.7
2.5×10^{11}	385.4	404.2	390.0	385.4

4.6.2. Effect of temperature on yield point

Table 4.5 shows the yield point values of MG and GMCs at temperature of 100 K, 300K and 500 K. As the temperature is increased bond between atoms become weak and they move far away so gets deformed easily. This results in a decrease in yield point as well as maximum load value with temperature rise. This trend is also observed in the studies of Lee et al. [93]. Composites have a higher yield point value as compared to the metallic glass at different temperatures. This could be due to the obstruction caused to movement of atoms in the glass matrix by nano-crystallites [94].

Table 4.5. Yield point values of $Zr_{50}Cu_{50}$ metallic glass and composites at different temperature of 100 K, 300K, 500 and strain rate of $2.5\times10^{10}\ s^{-1}$

Temperature (K)	Yield point (nN)			
	Metallic glass	Composite-I	Composite-II	Composite-III
100	51	77.1	60	65
300	22.1	60	50	48.3
500	6.7	60	64	51.8

Table 4.6. Comparing load value of present study with literature at a particular indentation depth and temperature.

References	Qiu et al.,2014 [50]	Wang et al., 2010 [63]	Paduraru et al., 2010 [95]	Present study		
Alloy system	$Cu_{50}Zr_{50}$	$Zr_{47}Cu_{31}Al_{13}Ni_{9}$	$Cu_{0.50}Zr_{0.50}$	$Zr_{50}Cu_{50}$		
Potential	LJ	TB-SMA	EMT	EAM		
Box size ($Å^3$)/atoms	210×150×120	160×160×124/ 200000	529×529×160/ 270000	100×100×100		
Indenter type/radius (Å)	Spherical/40	Conical	Cylindrical/ 300	Spherical/20		
Strain rate (s^{-1})	0.7×10^{10}	1.37×10^{9}	5.6×10^{8}	2.5×10^{10}		
Temperature (K)	293 and 500	300 and 600	116	300 and 500		100
Load(nN)	320 and 280	290 and 210	280	87 & 86.8	100 & 85	110
Indentation depth (Å)	25	40	42	25	40	

Table 4.6 shows the comparison of load of literature results with present study at a particular depth of indentation and different temperatures of working in case of $Zr_{50}Cu_{50}$ metallic glass. The difference in values may be due to indenter size, potential used and the box dimensions.

4.6.3. Effect of strain rate on hardness

It is found that in all the alloys there is an increase in hardness with increase in depth of indentation from 25 Å to 35 Å at all strain rates. The same trend was observed in the nano-indentation studies of Qiu et al., 2014 and Chu et al., 2012,[50, 96].The values obtained from the present study are represented in Tables 4.7, 4.8 and 4.9. As seen from Table 4.7 there is not much effect of presence of crystallites on hardness when compared with metallic glass. At 30 Å and 35 Å of indentation depth, composites have high hardness values as compared to MG sample at strain rate of $2.5\times10^{9}s^{-1}$ and $2.5\times10^{10}s^{-1}$. But, as strain rate is increased to

1.25×10^{11} s^{-1} and $2.5\times10^{11}s^{-1}$ there is decrease in for GMCs as compared to MG sample (Table 4.8 and 4.9).

Table 4.7. Hardness of $Zr_{50}Cu_{50}$ MG and GMCs at varying strain rates at a depth of 25 Å

Strain rate (s^{-1})	Hardness (GPa)				
	Metallic Glass		Composite-I	Composite-II	Composite-III
	Present study	Literature			
2.5×10^{9}	6.5		5.9	6.4	6.4
2.5×10^{10}	7	7.16 [50]	7.3	6.8	7.3
1.25×10^{11}	14.6		14.4	13.7	13.9
2.5×10^{11}	29		29.6	27.8	30.1

Hardness value of MG found in the present study is 7 GPa at a depth of 25 Å which is close to the observed nano-indentation simulation results (~7 GPa) of Qiu et al. [50].

Table 4.8. Hardness of $Zr_{50}Cu_{50}$ MG and GMCs at varying strain rates at a depth of 30 Å

Strain rate (s^{-1})	Hardness (GPa)			
	Metallic Glass	Composite- I	Composite- II	Composite III
2.5×10^{9}	7.7	8.2	8.4	9.3
2.5×10^{10}	9.4	12.6	11.3	11.2
1.25×10^{11}	17.9	16.3	16.4	15.0
2.5×10^{11}	35.6	29.5	30.6	33.4

Table 4.9. Hardness of $Zr_{50}Cu_{50}$ MG and GMCs at varying strain rates at a depth of 35 Å

Strain rate (s^{-1})	Hardness (GPa)			
	Metallic Glass	Composite- I	Composite- II	Composite III
2.5×10^{9}	15.3	14.9	16	16
2.5×10^{10}	17.4	20.2	18.3	17.8
1.25×10^{11}	30.7	26.2	24.8	26.5
2.5×10^{11}	63.7	52.4	53.1	49.7

4.6.4. Effect of temperature on hardness

Tables 4.10, 4.11 and 4.12 show the values of hardness of MG and GMCs at different depths of indentation as a function of temperature. It can be seen that hardness decreases with increase of temperature for both MG and GMCs. The same trend of decrease in hardness with temperature can be observed in the simulation work of Prasad et al. [97]. Hardness remains approximately constant with varying crystallite volume fraction in composites.

Table 4.10 Hardness of $Zr_{50}Cu_{50}$ based MG and GMCs at varying temperature at 25 Å depth

Temperature (K)	Hardness (GPa)			
	Metallic glass	Composite-I	Composite-II	Composite -III
100	7.2	7.6	8.1	8.3
300	7.2	7.3	7.3	7.4
500	6.9	7.2	6.4	8.3

Table 4.11 Hardness of $Zr_{50}Cu_{50}$ based MG and GMCs at varying temperature at 30 Å depth

Temperature (K)	Hardness (GPa)			
	Metallic glass	Composite-I	Composite-II	Composite -III
100	9.9	12.8	14.2	11.9
300	9.9	12.3	8.9	11.1
500	8.8	10.9	12.7	10.6

Table 4.12 Hardness of $Zr_{50}Cu_{50}$ based MG and GMCs at varying temperature at 35 Å depth

Temperature (K)	Hardness (GPa)			
	Metallic glass	Composite-I	Composite-II	Composite -III
100	18.7	19.4	19.4	19.6
300	17.3	19.2	16.7	17.4
500	16.5	17.1	16	18.3

4.7. Mechanical property of $Zr_{50}Cu_{30}Al_{20}$ based MG and GMCs

4.7.1. Effect of strain rate on the yield point and maximum load

With increasing strain rate, the yield point value shows an increase in metallic glass as well as that of composite-IV, V and VI as shown in Table 4.13. It is observed that with addition of Al to Zr-Cu yield point is lowered. Further, there is no trend observed on the yield point in the GMCs. Table 4.14 shows the maximum load values of MG and GMCs at different strain rates. It is observed that GMCs exhibit higher load bearing capacity than the MG at all strain rates. Also, the load bearing capacity is the highest for the GMC with maximum crystalline volume fraction.

Table 4.13. Yield point values for $Zr_{50}Cu_{30}Al_{20}$ based MG and GMCs at different strain rates

Strain rate (s^{-1})	Yield point (nN)			
	Metallic glass	Composite-IV	Composite-V	Composite-VI
2.5×10^{9}	24.3	29.5	16.0	19.0
2.5×10^{10}	44.6	49.6	26.2	44.1
1.25×10^{11}	94.2	97.1	139.5	148.9
2.5×10^{11}	263.4	276.6	355.7	310.5

Table 4.14. Maximum load values for $Zr_{50}Cu_{30}Al_{20}$ based MG and GMCs at different strain rates

Strain rate (s^{-1})	Maximum load value (nN)			
	Metallic glass	Composite-IV	Composite-V	Composite-VI
2.5×10^{9}	60.4	73.1	64.2	78.8
2.5×10^{10}	83.3	84.4	93.7	89.7
1.25×10^{11}	131.7	129.3	175.8	184.4
2.5×10^{11}	304	304.3	401.3	421.5

4.7.2. Effect of strain rate on the hardness

Hardness of $Zr_{50}Cu_{30}Al_{20}$ MG and GMCs are shown in Table 4.15 at a depth of 35 Å at varying strain rates and at a temperature of 300 K. It can be observed that hardness is increasing with strain rate value. The hardness value of literature work of Wang et al., [62] on $(Cu_{50}Zr_{50})_{88}Al_{12}$ metallic glass reveal a hardness value of 5.2 GPa. The variation may be due to strain rate used i.e., 0.8×10^{9} s^{-1}, potential used (LJ potential), Box size (320 ×320 ×320 $Å^{3}$).

Table 4.15 Hardness of $Zr_{50}Cu_{50}Al_{50}$ based MG and GMCs at varying strain rates at 35 Å depth

Strain rate (s^{-1})	Hardness (GPa)				
	Metallic Glass		Composite-IV	Composite-V	Composite-VI
	Present study	Literature [62]			
2.5×10^{9}	9.7	5.2	12.0	9.6	11.8
2.5×10^{10}	13.1		14.5	15.7	11.8
1.25×10^{11}	22.4		19.6	31.5	29.6
2.5×10^{11}	40.0		42.4	54.6	51.1

4.8. Variation of potential energy with displacement of indenter

A relationship between Potential energy and displacement of indenter in the $Zr_{50}Cu_{50}$ amorphous alloy sample has been explained with the plot at different strain rates of indentation as shown in Fig.4.27.

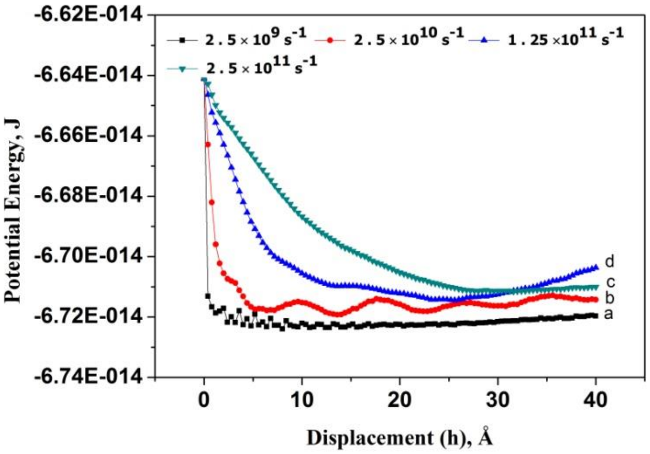

Figure 4.27. Potential energy vs. displacement of indenter plot at strain rates (a) $2.5\times10^{9}s^{-1}$ (b) $2.5\times10^{10}s^{-1}$ (c) $1.25\times10^{11}s^{-1}$ (d) $2.5\times10^{11}s^{-1}$

It is observed that there is a sharp fall in potential energy for the alloy when strain rate is 2.5×10^{9} s^{-1}. Further increase in strain rates (2.5×10^{10} s^{-1}, 1.25×10^{11} s^{-1}, 2.5×10^{11} s^{-1}) shows a gradually falling behaviour in plot [98]. It shows that elastic and plastic energy increases with increase in strain rate [50]. So, amorphous $Zr_{50}Cu_{50}$ alloy indented at high strain rate can bear high loading for a longer depth of indentation. Also, potential energy increase slowly but fluctuates more prominently with decrease in strain rate. It shows that potential energy versus displacement curve is also rate dependent.

CHAPTER 5

CONCLUSIONS AND SCOPE FOR FUTURE WORK

5.1. Conclusions

a) Zr-based MGs exhibit higher yield and maximum load with increase in strain rate. This is attributed to the displacement of atoms to a larger distance at high strain rates so that they cannot return to their position in a short time. Thus, the resistance to deformation increases. The rise of strain rate thus leads to hardening of sample and thus an increase in maximum load value.

b) Zr-based GMCs exhibit higher yield and maximum load as compared to MG with same composition as the strain rate is increased. This is attributed to obstruction to the movement of atoms in the glass matrix by the nano-crystallites and the delay in load transfer from matrix to crystallites at higher strain rates.

c) In $Zr_{50}Cu_{50}$ GMCs the maximum load increases with increase in crystalline volume fraction at low strain rates (2.5×10^{9} s^{-1} , 2.5×10^{10} s^{-1}) while decreases at high strain rates (1.25×10^{11} s^{-1}, 2.5×10^{11} s^{-1}). As the strain rate is increased along with crystallite volume fraction, crystallites get deformed too till the yield point is reached. So, the maximum load value decreases. Also, this is the reason that strain hardening decreases with increase in volume fraction of crystallites.

d) Amorphization of the crystallites occur with progress of deformation at all strain rates in GMCs as seen from the CSP analysis of $Zr_{50}Cu_{50}$ GMCs. This amorphization rate is reduced as the strain rate is increased.

e) Serrations are irregularly spaced in the load-displacement curves due to short range order of amorphous alloys.

f) Amplitude of serrations fluctuate about a certain load at higher strain rates (2.5×10^{11} s^{-1}) in case of $Zr_{50}Cu_{50}$ MG and GMCs and then load value decreases. This is attributed to strain softening phenomena.

g) Hardness increases with increase of strain rate as well as depth of indentation for all Zr-based MG and GMCs. This may be due to increase in load more distinctly with strain rate rise.

h) Composite containing single-crystallite has higher yield point value and maximum load as compared to that of composite with multi-spherical crystallites for the same crystallite volume fraction. This could be due to strong resistance against deformation from a monolithic crystallite.

i) Composites containing continuous cylindrical crystallites bear a higher load than that of composite containing spherical crystallites of same volume fraction of crystallites. This could be due to continuous reinforcement provided by composite containing cylindrical crystallites.

j) There is sharp fall in potential energy with decrease in strain rate.

5.2. Scope for future work

a) Stress distribution analysis at the crystallite sites.

b) Interface strength between crystallite and metallic glass.

c) Analysis of defects in the crystallite during deformation such as dislocation partials, twins and stacking faults.

References

[1] T. R. Anantharaman, *Metallic glasses: production, properties and applications*. Trans Tech Publications, 1984.

[2] W. Klement, R. H. Willens, and P. Duwez, “Non-crystalline Structure in Solidified Gold–Silicon Alloys,” *Nature*, vol. 187, no. 4740, pp. 869–870, Sep. 1960.

[3] A. Inoue, *Bulk Amorphous Alloys: Preparation and Fundamental Characteristics*. Trans Tech Publications, 1998.

[4] W. L. Johnson, A. Inoue, and C. T. Liu, *Bulk Metallic Glasses:* Cambridge University Press, 1999.

[5] G. Y. Sun, G. Chen, and G. L. Chen, “Comparison of microstructures and properties of Zr-based bulk metallic glass composites with dendritic and spherical bcc phase precipitates,” *Intermetallics*, vol. 15, no. 5–6, pp. 632–634, May 2007.

[6] R. D. Conner, H. Choi-Yim, and W. L. Johnson, “Mechanical properties of Zr57Nb5Al10Cu15.4Ni12.6 metallic glass matrix particulate composites,” *J. Mater. Res.*, vol. 14, no. 08, pp. 3292–3297, 1999.

[7] K.-W. Chen, S.-R. Jian, P.-J. Wei, J. S.-C. Jang, and J.-F. Lin, “A study of the relationship between semi-circular shear bands and pop-ins induced by indentation in bulk metallic glasses,” *Intermetallics*, vol. 18, no. 8, pp. 1572–1578, Aug. 2010.

[8] G. P. Zheng and Y. Shen, “Simulation of shear banding and crack propagation in bulk metallic glass matrix composites,” *J. Alloys Compd.*, vol. 509, Supplement 1, pp. S136–S140, Jun. 2011.

[9] D. C. Hofmann, J.-Y. Suh, A. Wiest, G. Duan, M.-L. Lind, M. D. Demetriou, and W. L. Johnson, “Designing metallic glass matrix composites with high toughness and tensile ductility,” *Nature*, vol. 451, no. 7182, pp. 1085–1089, Feb. 2008.

[10] A. Inoue and A. Takeuchi, “Recent development and application products of bulk glassy alloys,” *Acta Mater.*, vol. 59, no. 6, pp. 2243–2267, Apr. 2011.

[11] C. A. Schuh and T. G. Nieh, “A nanoindentation study of serrated flow in bulk metallic glasses,” *Acta Mater.*, vol. 51, no. 1, pp. 87–99, Jan. 2003.

[12] Y. F. Xue, H. N. Cai, L. Wang, F. C. Wang, and H. F. Zhang, “Dynamic compressive deformation and failure behavior of Zr-based metallic glass reinforced porous tungsten composite,” *Mater. Sci. Eng. A*, vol. 445–446, pp. 275–280, Feb. 2007.

[13] W. H. Wang, P. W. Z. Bian, Y. Zhang, M. X. Pan, and D. Q. Zhao, “Role of addition in formation and properties of Zr-based bulk metallic glasses,” *Intermetallics*, vol. 10, no. 11–12, pp. 1249–1257, Nov. 2002.

[14] A. S. Argon, “Plastic deformation in metallic glasses,” *Acta Metall.*, vol. 27, no. 1, pp. 47–58, Jan. 1979.

[15] F. Spaepen, “A microscopic mechanism for steady state inhomogeneous flow in metallic glasses,” *Acta Metall.*, vol. 25, no. 4, pp. 407–415, Apr. 1977.

[16] S. Y. Jiang, M. Q. Jiang, L. H. Dai, and Y. G. Yao, “Atomistic Origin of Rate-Dependent Serrated Plastic Flow in Metallic Glasses,” *Nanoscale Res. Lett.*, vol. 3, no. 12, pp. 524–529, Dec. 2008.

[17] F. Delogu, “Molecular dynamics of shear transformation zones in metallic glasses,” *Intermetallics*, vol. 16, no. 5, pp. 658–661, May 2008.

[18] S. Ogata, F. Shimizu, J. Li, M. Wakeda, and Y. Shibutani, “Atomistic simulation of shear localization in Cu–Zr bulk metallic glass,” *Intermetallics*, vol. 14, no. 8–9, pp. 1033–1037, Aug. 2006.

[19] E. F. Kyoung-Won Park, “Deformation behaviors under tension and compression: Atomic simulation of Cu65Zr35 metallic glass,” *Intermetallics*, vol. 19, no. 8, pp. 1168–1173, 2011.

[20] R. H. Doremus, “Structure of Inorganic Glasses,” *Annu. Rev. Mater. Sci.*, vol. 2, no. 1, pp. 93–120, 1972.

[21] M. Abdel-Baki and F. El-Diasty, “Optical properties of oxide glasses containing transition metals: Case of titanium- and chromium-containing glasses,” *Curr. Opin. Solid State Mater. Sci.*, vol. 10, no. 5–6, pp. 217–229, Oct. 2006.

[22] M. Telford, “The case for bulk metallic glass,” *Mater. Today*, vol. 7, no. 3, pp. 36–43, Mar. 2004.

[23] J. F. Löffler, “Bulk metallic glasses,” *Intermetallics*, vol. 11, no. 6, pp. 529–540, Jun. 2003.

[24] S. Pauly, J. Das, C. Duhamel, and J. Eckert, “Martensite Formation in a Ductile Cu47.5Zr47.5Al5 Bulk Metallic Glass Composite,” *Adv. Eng. Mater.*, vol. 9, no. 6, pp. 487–491, 2007.

[25] Y. Shi and M. L. Falk, “A computational analysis of the deformation mechanisms of a nanocrystal–metallic glass composite,” *Acta Mater.*, vol. 56, no. 5, pp. 995–1000, Mar. 2008.

[26] D. C. Hofmann, “Bulk Metallic Glasses and Their Composites: A Brief History of Diverging Fields,” *J. Mater.*, vol. 2013, p. e517904, Jan. 2013.

[27] F. Szuecst, C. P. Kim, and W. L. Johnson, “Mechanical properties of Zr56.2Ti13.8Nb5.0Cu6.9Ni5.6Be12.5 ductile phase reinforced bulk metallic glass composite,” *Acta Mater.*, vol. 49, no. 9, pp. 1507–1513, 2001.

[28] Y. Q. Cheng and E. Ma, “Atomic-level structure and structure–property relationship in metallic glasses,” *Prog. Mater. Sci.*, vol. 56, no. 4, pp. 379–473, May 2011.

[29] J. Basu and S. Ranganathan, “Bulk metallic glasses: A new class of engineering materials,” *Sadhana*, vol. 28, no. 3–4, pp. 783–798, Jun. 2003.

[30] P. G. Debenedetti and F. H. Stillinger, “Supercooled liquids and the glass transition,” *Nature*, vol. 410, no. 6825, pp. 259–267, Mar. 2001.

[31] Z. P. Lu and C. T. Liu, “A new glass-forming ability criterion for bulk metallic glasses,” *Acta Mater.*, vol. 50, no. 13, pp. 3501–3512, Aug. 2002.

[32] A. Inoue, X. M. Wang, and W. Zhang, “Developments and applications of bulk metallic glasses,” *Rev Adv Mater Sci*, vol. 18, pp. 1–9, 2008.

[33] R. Nowosielski, A. Januszka, and R. Babilas, “Thermal properties of Fe-based bulk metallic glasses,” *J. Achiev. Mater. Manuf. Eng.*, vol. 55, no. 2, pp. 349–354, 2012.

[34] C. V. Gokularathnam, “Structure of metallic glasses,” *J. Mater. Sci.*, vol. 9, no. 4, pp. 673–682, Apr. 1974.

[35] H. Chen, “Metallic glasses,” *Chin. J. Phys.*, vol. 28, no. 5, pp. 407–425, 1990.

[36] D. Turnbull, “Metastable structures in metallurgy,” *Metall. Trans. B*, vol. 12, no. 2, pp. 217–230, Jun. 1981.

[37] E. J. Lavernia and Y. Wu, *Spray atomization and deposition*. Wiley New York, 1996.

[38] B. R. Rao, “Bulk Metallic Glasses: Materials of Future,” 2009.

[39] C. Suryanarayana and A. Inoue, *Bulk Metallic Glasses*. CRC Press, 2011.

[40] A. Inoue, K. Kita, T. Zhang, and T. Masumoto, “An amorphous La55Al25Ni20 alloy prepared by water quenching,” *Mater. Trans. JIM*, vol. 30, no. 9, pp. 722–725, 1989.

[41] A. Inoue, T. Nakamura, N. Nishiyama, and T. Masumoto, “Mg-Cu-Y bulk amorphous alloys with high tensile strength produced by a high-pressure die casting method,” *Mater. Trans. JIMJapan*, vol. 33, no. 10, pp. 937–945, 1992.

[42] C. Suryanarayana, “Mechanical alloying and milling,” *Prog. Mater. Sci.*, vol. 46, no. 1–2, pp. 1–184, Jan. 2001.

[43] A. I. Salimon, M. F. Ashby, Y. Bréchet, and A. L. Greer, “Bulk metallic glasses: what are they good for?,” *Mater. Sci. Eng. A*, vol. 375–377, pp. 385–388, Jul. 2004.

[44] W. H. Wang, C. Dong, and C. H. Shek, “Bulk metallic glasses,” *Mater. Sci. Eng. R Rep.*, vol. 44, no. 2–3, pp. 45–89, Jun. 2004.

[45] H. J. Leamy, T. T. Wang, and H. S. Chen, “Plastic flow and fracture of metallic glass,” *Metall. Trans.*, vol. 3, no. 3, pp. 699–708, Mar. 1972.

[46] J. Lu, G. Ravichandran, and W. L. Johnson, “Deformation behavior of the Zr41.2Ti13.8Cu12.5Ni10Be22.5 bulk metallic glass over a wide range of strain-rates and temperatures,” *Acta Mater.*, vol. 51, no. 12, pp. 3429–3443, 2003.

[47] W. c. Oliver and G. m. Pharr, “An improved technique for determining hardness and elastic modulus using load and displacement sensing indentation experiments,” *J. Mater. Res.*, vol. 7, no. 06, pp. 1564–1583, 1992.

[48] C. Heinrich, A. M. Waas, and A. S. Wineman, “Determination of material properties using nanoindentation and multiple indenter tips,” *Int. J. Solids Struct.*, vol. 46, no. 2, pp. 364–376, Jan. 2009.

[49] I. N. Sneddon, “The relation between load and penetration in the axisymmetric boussinesq problem for a punch of arbitrary profile,” *Int. J. Eng. Sci.*, vol. 3, no. 1, pp. 47–57, May 1965.

[50] C. Qiu, P. Zhu, F. Fang, D. Yuan, and X. Shen, “Study of nanoindentation behavior of amorphous alloy using molecular dynamics,” *Appl. Surf. Sci.*, vol. 305, pp. 101–110, Jun. 2014.

[51] W. Zhang and A. Inoue, “High glass-forming ability and good mechanical properties of new bulk glassy alloys in Cu–Zr–Ag ternary system,” *J. Mater. Res.*, vol. 21, no. 01, pp. 234–241, 2006.

[52] K. b. Kim, J. Das, M. h. Lee, S. Yi, E. Fleury, Z. f. Zhang, W. h. Wang, and J. Eckert, “Propagation of shear bands in a Cu47.5Zr47.5Al5 bulk metallic glass,” *J. Mater. Res.*, vol. 23, no. 01, pp. 6–12, 2008.

[53] S.-W. Lee, M.-Y. Huh, E. Fleury, and J.-C. Lee, “Crystallization-induced plasticity of Cu–Zr containing bulk amorphous alloys,” *Acta Mater.*, vol. 54, no. 2, pp. 349–355, Jan. 2006.

[54] T. Wada, T. Zhang, and A. Inoue, “Formation and high mechanical strength of bulk glassy alloys in Zr-Al-Co-Cu system,” *Mater. Trans.*, vol. 44, no. 9, pp. 1839–1844, 2003.

[55] J. Fornell, A. Concustell, S. Suriñach, W. H. Li, N. Cuadrado, A. Gebert, M. D. Baró, and J. Sort, “Yielding and intrinsic plasticity of Ti–Zr–Ni–Cu–Be bulk metallic glass,” *Int. J. Plast.*, vol. 25, no. 8, pp. 1540–1559, Aug. 2009.

[56] C. Tang, Y. Li, and K. Zeng, “Characterization of mechanical properties of a Zr-based metallic glass by indentation techniques,” *Mater. Sci. Eng. A*, vol. 384, no. 1–2, pp. 215–223, Oct. 2004.

[57] W. J. Wright, R. Saha, and W. D. Nix, “Deformation mechanisms of the Zr40Ti14Ni10Cu12Be24 bulk metallic glass,” *Mater. Trans.-JIM*, vol. 42, no. 4, pp. 642–649, 2001.

[58] J. Sort, N. Van Steenberge, A. Gimazov, A. Concustell, S. Suriñach, A. Gebert, J. Eckert, and M. D. Baró, “Study of the Mechanical Behaviour of a Zr-Based Metallic Glass Rod Using Micro- and Nano-Indentation,” *Open Mater. Sci. J.*, vol. 2, pp. 1–5, 2008.

[59] U. Ramamurty, S. Jana, Y. Kawamura, and K. Chattopadhyay, “Hardness and plastic deformation in a bulk metallic glass,” *Acta Mater.*, vol. 53, no. 3, pp. 705–717, Feb. 2005.

[60] L. Wang, H. Bei, Y. F. Gao, Z. P. Lu, and T. G. Nieh, “Effect of residual stresses on the hardness of bulk metallic glasses,” *Acta Mater.*, vol. 59, no. 7, pp. 2858–2864, 2011.

[61] M. Heilmaier and J. Eckert, “The synthesis and properties of Zr-based metallic glasses and glass-matrix composites,” *JOM*, vol. 52, no. 7, pp. 43–47, Jul. 2000.

[62] Y.-C. Wang and C.-Y. Wu, “Molecular dynamics simulation of Cu-Zr-Al metallic-glass films under indentation,” *Thin Solid Films*, vol. 561, pp. 114–119, Jun. 2014.

[63] Y.-C. Wang, C.-Y. Wu, J. P. Chu, and P. K. Liaw, “Indentation Behavior of Zr-Based Metallic-Glass Films via Molecular-Dynamics Simulations,” *Metall. Mater. Trans. A*, vol. 41, no. 11, pp. 3010–3017, Jul. 2010.

[64] D. Şopu, Y. Ritter, H. Gleiter, and K. Albe, “Deformation behavior of bulk and nanostructured metallic glasses studied via molecular dynamics simulations,” *Phys. Rev. B*, vol. 83, no. 10, p. 100202, Mar. 2011.

[65] H. Okamoto, “Cu-Zr (Copper-Zirconium),” *J. Phase Equilibria Diffus.*, vol. 29, no. 2, pp. 204–204, Apr. 2008.

[66] M. P. Allen, “Introduction to molecular dynamics simulation,” *Comput. Soft Matter Synth. Polym. Proteins*, vol. 23, pp. 1–28, 2004.

[67] E. C. Neyts and A. Bogaerts, “Combining molecular dynamics with Monte Carlo simulations: implementations and applications,” in *Theoretical Chemistry in Belgium*, B. Champagne, M. S. Deleuze, F. D. Proft, and T. Leyssens, Eds. Springer Berlin Heidelberg, 2014, pp. 277–288.

[68] B. J. Alder and Te. Wainwright, “Phase transition for a hard sphere system,” *J. Chem. Phys.*, vol. 27, no. 5, pp. 1208–1209, 1957.

[69] A. Rahman, “Correlations in the Motion of Atoms in Liquid Argon,” *Phys. Rev.*, vol. 136, no. 2A, pp. A405–A411, Oct. 1964.

[70] F. F. Abraham, R. Walkup, H. Gao, M. Duchaineau, T. D. D. L. Rubia, and M. Seager, “Simulating materials failure by using up to one billion atoms and the world’s fastest computer: Work-hardening,” *Proc. Natl. Acad. Sci.*, vol. 99, no. 9, pp. 5783–5787, Apr. 2002.

[71] M. S. Daw and M. I. Baskes, “Embedded-atom method: Derivation and application to impurities, surfaces, and other defects in metals,” *Phys. Rev. B*, vol. 29, no. 12, pp. 6443–6453, Jun. 1984.

[72] J. E. Jones, “On the determination of molecular fields. II. From the equation of state of a gas,” *Proc. R. Soc. Lond. Ser. Contain. Pap. Math. Phys. Character*, pp. 463–477, 1924.

[73] D. W. Brenner, “Empirical potential for hydrocarbons for use in simulating the chemical vapor deposition of diamond films,” *Phys. Rev. B*, vol. 42, no. 15, pp. 9458–9471, Nov. 1990.

[74] M. I. Mendelev, D. J. Sordelet, and M. J. Kramer, "Using atomistic computer simulations to analyze x-ray diffraction data from metallic glasses," *J. Appl. Phys.*, vol. 102, no. 4, p. 043501, Aug. 2007.

[75] M. W. Finnis and J. E. Sinclair, "A simple empirical N-body potential for transition metals," *Philos. Mag. A*, vol. 50, no. 1, pp. 45–55, 1984.

[76] G. Gilmer and S. Yip, "Basic Monte Carlo Models: Equilibrium and Kinetics," in *Handbook of Materials Modeling*, S. Yip, Ed. Springer Netherlands, 2005, pp. 613–628.

[77] M. Rao, C. Pangali, and B. J. Berne, "On the force bias Monte Carlo simulation of water: methodology, optimization and comparison with molecular dynamics," *Mol. Phys.*, vol. 37, no. 6, pp. 1773–1798, Jun. 1979.

[78] J. R. Chelikowsky, "Electronic Scale," in *Handbook of Materials Modeling*, S. Yip, Ed. Springer Netherlands, 2005, pp. 121–135.

[79] M. Ben-Nun and T. J. Martínez, "Ab Initio Quantum Molecular Dynamics," in *Advances in Chemical Physics*, I. Prigogine and S. A. Rice, Eds. John Wiley & Sons, Inc., 2002, pp. 439–512.

[80] S. Plimpton, "Fast parallel algorithms for short-range molecular dynamics," *J. Comput. Phys.*, vol. 117, no. 1, pp. 1–19, 1995.

[81] A. Stukowski, "Visualization and analysis of atomistic simulation data with OVITO–the Open Visualization Tool," *Model. Simul. Mater. Sci. Eng.*, vol. 18, no. 1, p. 015012, Jan. 2010.

[82] H. Zhou, S. Qu, and W. Yang, "An atomistic investigation of structural evolution in metallic glass matrix composites," *Int. J. Plast.*, vol. 44, pp. 147–160, May 2013.

[83] X. Hui, X. Liu, R. Gao, H. Hou, H. Fang, Z. Liu, and G. Chen, "Atomic structures of Zr-based metallic glasses," *Sci. China Ser. G Phys. Mech. Astron.*, vol. 51, no. 4, pp. 400–413, Apr. 2008.

[84] S.-W. Kao, C.-C. Hwang, and T.-S. Chin, "Simulation of reduced glass transition temperature of Cu–Zr alloys by molecular dynamics," *J. Appl. Phys.*, vol. 105, no. 6, p. 064913, 2009.

[85] Q. Wang, C. Dong, J. Qiang, and Y. Wang, "Cluster line criterion and Cu–Zr–Al bulk metallic glass formation," *Mater. Sci. Eng. A*, vol. 449–451, pp. 18–23, Mar. 2007.

[86] L. Ma, L. Levine, R. Dixson, D. Smith, and D. Bahr, "Effect of the Spherical Indenter Tip Assumption on the Initial Plastic Yield Stress," 2012.

[87] C. A. Schuh, "Nanoindentation studies of materials," *Mater. Today*, vol. 9, no. 5, pp. 32–40, May 2006.

[88] C.-Y. Wu, Y.-C. Wang, and C. Chen, "Indentation properties of Cu–Zr–Al metallic-glass thin films at elevated temperatures via molecular dynamics simulation," *Comput. Mater. Sci.*, vol. 102, pp. 234–242, May 2015.

[89] I. Szlufarska, R. K. Kalia, A. Nakano, and P. Vashishta, "Atomistic processes during nanoindentation of amorphous silicon carbide," *Appl. Phys. Lett.*, vol. 86, no. 2, pp. 021915–021915–3, Jan. 2005.

[90] C. A. Schuh, A. C. Lund, and T. G. Nieh, "New regime of homogeneous flow in the deformation map of metallic glasses: elevated temperature nanoindentation experiments and mechanistic modeling," *Acta Mater.*, vol. 52, no. 20, pp. 5879–5891, Dec. 2004.

[91] W. D. Callister and D. G. Rethwisch, *Materials Science and Engineering: An Introduction*, 8th Edition Binder Ready Version edition. Wiley, 2010.

[92] I. Szlufarska, “Atomistic simulations of nanoindentation,” *Mater. Today*, vol. 9, no. 5, pp. 42–50, May 2006.

[93] D.-G. Lee, Y. G. Kim, B. Hwang, S. Lee, and Y. T. Lee, “Effects of temperature on dynamic compressive properties of Zr-based amorphous alloy and composite,” *Mater. Sci. Eng. A*, vol. 472, no. 1–2, pp. 316–323, Jan. 2008.

[94] N. Yedla, M. Srinivas, S. Ghosh, and B. Majumdar, “Effect of nano-crystallization on the plasticity in Cu–Zr amorphous binary alloys,” *Intermetallics*, vol. 18, no. 12, pp. 2419–2424, Dec. 2010.

[95] A. Păduraru, U. G. Andersen, A. Thyssen, N. P. Bailey, K. W. Jacobsen, and J. Schiøtz, “Computer simulations of nanoindentation in Mg–Cu and Cu–Zr metallic glasses,” *Model. Simul. Mater. Sci. Eng.*, vol. 18, no. 5, p. 055006, Jul. 2010.

[96] J. P. Chu, J. S. C. Jang, J. C. Huang, H. S. Chou, Y. Yang, J. C. Ye, Y. C. Wang, J. W. Lee, F. X. Liu, P. K. Liaw, Y. C. Chen, C. M. Lee, C. L. Li, and C. Rullyani, “Thin film metallic glasses: Unique properties and potential applications,” *Thin Solid Films*, vol. 520, no. 16, pp. 5097–5122, Jun. 2012.

[97] K. Eswar Prasad, R. Raghavan, and U. Ramamurty, “Temperature dependence of pressure sensitivity in a metallic glass,” *Scr. Mater.*, vol. 57, no. 2, pp. 121–124, Jul. 2007.

[98] B. Bhushan, *Nanotribology and Nanomechanics: An Introduction*. Springer Science & Business Media, 2005.

BIO-DATA

Name	Ashwani Kumar
Date of birth	02.11.1988
Permanent Address	Madhopur, P.O.-Basudeopur Disst- Munger, Bihar, 811202
E-mail ID	ashwanik2010@gmail.com
Languages Known	Hindi, English

EDUCATIONAL QUALIFICATION

Examination	Discipline/ Specialization	School/college	Board/ University	Year of Passing	Percentage
M. Tech (Research)	Metallurgical and Materials Engineering	NIT Rourkela	National Institute of Technology Rourkela	2015	8.77 (CGPA)
B. Tech.	Mechanical Engineering	ITM, Gwalior	RGPV University, Bhopal	2011	69.16 %
HSC	Maths, Physics, Chemistry	SVM, Munger	CBSE	2005	57.4 %
SSC		Baldwin Academy, Patna	CBSE	2003	70 %

PROJECT DETAILS

M. Tech (Research)

Molecular Dynamics Simulation of Nano-indentation Studies on Zr-based Metallic Glass Matrix Composites

Conferences

a) **Ashwani Kumar**, N. Yedla, Structure property comparison of glass matrix composite and amorphous Cu-Zr alloy, NCPCM-2013 (NIT), Rourkela, India

b) **Ashwani Kumar**, N. Yedla, Molecular dynamics simulation studies of $Zr_{50}Cu_{50}$ metallic glass and glass Matrix composite under nano-indentation at varying strain rates , NCPCM-2014 (NIT),Rourkela, India.

Paper published in conference proceeding

Ashwani Kumar, N. Yedla, “Mechanical and structural studies of $Zr_{50}Cu_{50}$ glass matrix composite during nano indentation- a molecular dynamics study, IOP Conf. Series: Materials Science and Engineering, vol.75, no. 012020, 2015